



1 Presentation and discussion of the high resolution atmosphere-land 2 surface-subsurface simulation dataset of the virtual Neckar 3 catchment for the period 2007-2015

4 Bernd Schalge¹, Gabriele Baroni², Barbara Haese³, Daniel Erdal⁴, Gernot Geppert⁵, Pablo Saavedra¹,
5 Vincent Haefliger¹, Harry Vereecken^{6,7}, Sabine Attinger^{8,9}, Harald Kunstmann^{3,10}, Olaf A. Cirpka⁴, Felix
6 Ament¹¹, Stefan Kollet^{6,7}, Insa Neuweiler¹², Harrie-Jan Hendricks Franssen^{6,7}, Clemens Simmer^{1,7}

7 ¹Institute for Geosciences, University of Bonn, Bonn, Germany

8 ² Department of Agricultural and Food Sciences, University of Bologna, Bologna, Italy

9 ³Institute of Geography, University of Augsburg, Augsburg, Germany

10 ⁴Center for Applied Geoscience, University of Tübingen, Tübingen, Germany

11 ⁵Department of Meteorology, University of Reading, Reading, England

12 ⁶Forschungszentrum Jülich GmbH, Agrosphere (IBG-3), Jülich, Germany

13 ⁷Centre for High-Performance Scientific Computing (HPSC-TerrSys), Geoverbund ABC/J, Jülich, Germany

14 ⁸Institute of Earth and Environmental Science, University of Potsdam, Potsdam, Germany

15 ⁹Helmholtz-Center for Environmental Research, Leipzig, Germany

16 ¹⁰Institute of Meteorology and Climate Research (IMK-IFU), Karlsruhe Institute of Technology (KIT), Garmish-
17 Partenkirchen, Germany

18 ¹¹Meteorological Institute, University of Hamburg, Hamburg, Germany

19 ¹²Hannover, Institut für Strömungsmechanik und Umweltphysik im Bauwesen, Leibniz Universität Hannover, Germany

20
21 *Correspondence to:* Bernd Schalge (bschalge@uni-bonn.de)

22 **Abstract.**

23 Coupled numerical models, which simulate water and energy fluxes in the subsurface-land surface-atmosphere system in a
24 physically consistent way are a prerequisite for the analysis and a better understanding of heat and matter exchange fluxes at
25 compartmental boundaries and interdependencies of states across these boundaries. Complete state evolutions generated by
26 such models may be regarded as a proxy of the real world, provided they are run at sufficiently high resolution and incorporate
27 the most important processes. Such a virtual reality can be used to test hypotheses on the functioning of the coupled terrestrial
28 system. Coupled simulation systems, however, face severe problems caused by the vastly different scales of the processes
29 acting in and between the compartments of the terrestrial system, which also hinders comprehensive tests of their realism. We
30 used the Terrestrial Systems Modeling Platform TerrSysMP, which couples the meteorological model COSMO, the land-
31 surface model CLM, and the subsurface model ParFlow, to generate a virtual catchment for a regional terrestrial system



32 mimicking the Neckar catchment in southwest Germany. Simulations for this catchment are made for the period 2007-2015,
33 and at a spatial resolution of 400m for the land surface and subsurface and 1.1km for the atmosphere. Among a discussion of
34 modelling challenges, the model performance is evaluated based on real observations covering several variables of the water
35 cycle. We find that the simulated (virtual) catchment behaves in many aspects quite close to observations of the real Neckar
36 catchment, e.g. concerning atmospheric boundary-layer height, precipitation, and runoff. But also discrepancies become
37 apparent, both in the ability of the model to correctly simulate some processes which still need improvement such as overland
38 flow, and in the realism of some observation operators like the satellite based soil moisture sensors. The whole raw dataset is
39 available for interested users. The dataset described here is available via the CERA database (Schalge et al, 2020):
40 https://doi.org/10.26050/WDC/Neckar_VCS_v1

41

42 **1 Introduction**

43 Earth environmental models are becoming increasingly important for climate and weather prediction, flood forecasting, water
44 resources management, agriculture, and water quality control (e.g. Shrestha et al. 2014; Larsen et al. 2014; Simmer et al.,
45 2015). Assuming that the models are able to resemble the real-world based on state-of-the-art understanding of the system
46 processes, the models are also used as “virtual realities” for hypothesis testing and decision support systems in many scientific
47 disciplines (Clark et al., 2015, Semenova & Beven, 2015).

48 Virtual realities have been used for specific compartments of the terrestrial system in many studies (see Fatichi et al., 2016,
49 and reference herein) and several advantages have been recognized. Bashford et al. (2002) computed virtual remote-sensing
50 observations with 1 km resolution to derive, among others, process parameterizations for evapotranspiration in a hydrological
51 model operating on the same scale as the remote sensing data. Weiler and McDonnel (2004) used a virtual-reality approach on
52 the hill-slope scale to detect and quantify the major controls on subsurface flow processes and derive tunable parameters for
53 conceptual models. Virtual experiments allowed Schlueter et al. (2012) to explore the relationship between soil architecture
54 and hydraulic behavior and Chaney et al. (2015) to testing sampling designs. Hein et al. (2019) explores the relative importance
55 of different factors in the hydrologic response of a catchment. Virtual realities are also often used to overcome limitations on
56 the data-scarce observations. In this context, Ajami and Sharma (2018) used simulations results to test disaggregation method
57 for soil moisture observations. In subsurface hydrology it is a standard procedure to test inverse modeling and data-assimilation
58 approaches on virtual aquifers (e.g., Zimmermann et al., 1998; Hendricks Franssen et al., 2009), which are used to generate
59 realistic aquifer data with exactly known hydraulic and geochemical properties at every point (e.g., Schaefer et al., 2002).

60 More recently, it has been highlighted that the terrestrial systems should be better exploited by the use of integrated models
61 which are able to simulate water and energy fluxes in the subsurface-land surface-atmosphere system in a physically consistent
62 way (Clark et al., 2015, Davison et al, 2018). For this reason, these integrated modeling approaches have also been considered
63 to generate virtual realities (Mackay et al., 2015). However, despite the increasing computational capability and availability of



64 infrastructures, these modelling approaches are generally more technically demanding. In addition, the use of these types of
65 integrated models requires different expertises that are not usually cover within one single scientific group but requires strong
66 interdisciplinary collaborations among different partners. For these reasons, the use of these types of models is still not
67 commonly foreseen.

68 To overcome this limitation, in this paper we present the development, the testing and the data of a virtual reality of a mesoscale
69 catchment based on a fully integrated terrestrial model system. Our virtual catchment encompasses the terrestrial system from
70 the bedrock to the upper atmosphere covering the catchment of a higher-order river (length $\approx 380\text{km}$, area $\approx 14000\text{km}^2$)
71 including a buffer zone surrounding it, in which we simulate - as realistically as currently possible - the multi-year evolution
72 of states including the water and energy fluxes in and between all its compartments. We specifically venture to represent the
73 strong spatial variability of the land components, which affects the overall system behavior due to nonlinear couplings and
74 feedbacks. Since a virtual catchment with no resemblance to a real world catchment hardly allows for evaluating its realism,
75 we base our simulation loosely on the Neckar catchment in southwest Germany that contains quite variable topography,
76 different land cover, high and low precipitation regions, deep and low water tables and regions prone to flooding events. (see
77 Figure 1). The model does not aim at exactly reproducing the catchment's response to hydro-climatic forcing, instead we only
78 require that the simulated response is realistic with respect to typical spatial and temporal characteristics. For this reason, we
79 discuss the model realism in comparison with observations of the real catchment, but also its limitations, particularly in relation
80 to the chosen resolutions which balance the detail in process representation and computational feasibility

81 The remainder of the paper is structured as follows. In section 2, we introduce the simulation platform TerrSysMP, while
82 Section 3 describes in detail the surface and subsurface parameters for topography, soils and aquifers, land use, vegetation,
83 and the river network. In Section 4, we show snapshots and time series of state variables or system parameters extracted from
84 the virtual catchment and compare them to observations in the real Neckar catchment to demonstrate how well the most
85 important requirements are met. These results as well as possible ways to improve them are discussed in Section 5 together
86 with several issues, which came up during the development phase. We provide conclusions and an outlook in Section 6.

87 **2 The Terrestrial Systems Modeling Platform (TerrSysMP)**

88 We used the Terrestrial System Modeling Platform (TerrSysMP, see Shrestha et al. 2014; Gasper et al. 2014; Sulis et al. 2015)
89 developed within the Transregional Collaborative Research Centre TR32 (Simmer et al. 2015) for the generation of the virtual
90 catchment. TerrSysMP couples (Figure 2) the hydrologic flow model ParFlow v693 (Ashby and Falgout, 1996; Jones and
91 Woodward, 2001; Kollet and Maxwell, 2006), the land-surface model Community Land Model, CLM v3.5 (Oleson et al.,
92 2008), and the atmospheric model Consortium for Small Scale Modeling (COSMO v4.21, Baldauf et al., 2011) via the Ocean
93 Atmosphere Sea Ice Coupling framework OASIS3 (e.g. Valcke et al., 2006), using a dynamical two-way approach including
94 down- and upscaling algorithms for fluxes and state variables between computational grids of different resolution.



95 ParFlow is a variably saturated watershed flow model, which solves the three-dimensional Richards equation to model
96 saturated and unsaturated flow in the subsurface, and the fully integrated kinematic wave equation to model two-dimensional
97 overland flow. Also other global and regional hydrological models use the latter to route overland flow, e.g. MODCOU
98 (Haefliger et al., 2015) and TRIP (Alkama et al., 2012). Advanced Newton-Krylov multigrid solvers are used that are especially
99 suitable for massively parallel computer environments. Excellent model performance and parallel efficiency have been
100 documented by Jones and Woodward (2001), Kollet and Maxwell (2006), and Kollet et al. (2010). A unique feature of ParFlow
101 is the use of an advanced octree data structure for rendering overlapping objects in 3-D space, which facilitates modeling
102 complex geology and heterogeneity as well as the representation of topography based on digital elevation models and
103 watershed boundaries.

104 CLM is a single column biogeophysical land-surface model released by the National Center for Atmospheric Research
105 (NCAR), which considers coupled snow, soil, and vegetation processes. Land surface heterogeneity is represented as a nested
106 sub-grid hierarchy in which grid cells are composed of multiple land units (glacier, lake, wetland, urban, and vegetation),
107 snow/soil columns (to capture variability in snow and soil states within each land unit), and Plant Functional Types (PFTs) to
108 capture the biogeophysical and biogeochemical differences between broad categories of plants in terms of their functional
109 characteristics. In TerrSysMP, the 1-D Richards-equation model included in CLM is replaced by ParFlow.

110 COSMO is a limited-area, non-hydrostatic numerical weather prediction model, which operationally runs at the German
111 weather service DWD, among others, for Numerical Weather Prediction (NWP) and various scientific applications on the
112 meso- β and meso- γ scale. COSMO is based on the primitive thermo-hydrodynamical equations describing compressible flow
113 in a moist atmosphere. As a limited-area model, COSMO needs lateral boundary conditions from a driving larger-scale model.
114 We impose the lateral conditions by nesting COSMO in COSMO-DE which spans Germany. At the lateral boundaries a
115 relaxation technique is used in which the internal model solution is nudged against an externally specified solution over a
116 narrow transition zone between the two domains.

117 Within OASIS3, the upscaling algorithm uses the mosaic or explicit sub-grid approach (Avisar and Pielke, 1989) in which
118 high-resolution land surface fluxes are averaged and transferred to the coarser resolution of the atmospheric model component.
119 The implemented Schomburg scheme (Schomburg et al., 2010, 2012) downscales atmospheric variables of the lowest
120 atmospheric model layer to the higher-resolved land surface model. The scheme involves (i) spline interpolation while
121 conserving mean and lateral gradients of the coarse field, (ii) deterministic downscaling rules to exploit empirical relationships
122 between atmospheric variables and surface variables, and (iii) the addition of high-resolution variability (i.e. noise) in order to
123 honor the non-deterministic part and to restore spatial variability.

124 TerrSysMP allows simulating the terrestrial water, energy, and biogeochemical cycles from the deeper subsurface including
125 groundwater (ParFlow) across the land-surface (CLM) into the atmosphere (COSMO). Water and energy cycles are coupled
126 via evaporation and plant transpiration; these processes are modeled by CLM with a non-linear coupling to ParFlow through
127 soil-water availability and root-water uptake (Figure 2). The two-way coupling between CLM and COSMO encompasses
128 radiation exchange and turbulent exchanges of moisture, energy, and momentum. OASIS3 allows for different temporal and



129 spatial resolutions of the coupled model components. For example, a temporal resolution of 15 minutes is sufficient for the
130 subsurface and land-surface components, whereas time steps as small as 5 seconds are needed for the atmosphere. A higher
131 spatial resolution can be assigned for the surface and subsurface parts to allow for a better representation of soil and land-use
132 heterogeneity.

133 Since high-resolution and long time-series of the fully coupled system are needed to satisfy our need to check the statistical
134 behavior of the system, the models were run on the IBM/BlueGeneQ System JUQUEEN at the Jülich Supercomputing Centre
135 (Jülich Supercomputing Centre, 2015). JUQUEEN has a total of 28672 nodes with 16 cores each. Our configuration involved
136 using 256 nodes for 12hours, restarting the simulation every 7 simulation days. This is necessary as the runtime for Parflow
137 can vary greatly depending on the conditions in the virtual catchment. The total number of grid cells for the domain is 323,675
138 per model layer with 10 layers for CLM and 50 layers for ParFlow, and 58,420 grid-points for the 50 COSMO layers resulting
139 in 22.3 million grid cells. We ran the fully-coupled model for a total period of nine years (2007-2015). On average the actual
140 runtime was approximately eight hours. This means that for one year of simulation about 1.7 million core-hours are needed.
141 For the full nine-year time-series that is about 12 million core-hours; another ~8 million hours were needed for the spin-up.
142 We used an output interval of 15 minutes, which results in a total output of 38.5TB of data for the full time-series, where about
143 half was produced by COSMO and a quarter each by CLM and ParFlow.

144 **3 Description of the Virtual Catchment**

145 Our virtual catchment is based on the Neckar catchment in southwestern Germany (see Figure 1), east of the Black Forest
146 mountain range and north of the Jurassic ridge of the Swabian Alb. The catchment has a varying topography including
147 mountains up to 1050 m a.s.l., river valleys, different land use types, i.e. grassland, cropland (majority of the area), broadleaf
148 and needle leaf forest (see Figure 3), and relatively large soil spatial variability. Annual mean precipitation over the real
149 catchment ranges between 500 and 2000mm (see Section 5.1) with highest values over the Black Forest. Inter-annual
150 variability of precipitation can reach up to one third of the mean value. Monthly precipitation can vary largely and its mean
151 annual cycle is weak with slightly lower values in spring and autumn. While summer precipitation is dominated by convection,
152 winter precipitation is predominantly related to fronts of extra-tropical cyclones with enhanced precipitation over the
153 mountains due to orographic lift. Daily average temperatures vary with altitude between -5°C and 0°C in January and between
154 13 and 18°C in July. Land use and cover in the lower elevations are dominated by agriculture while the Black Forest features
155 mainly needle-leaf trees. Broad-leaf trees can be found over smaller areas throughout the catchment. The distance to
156 groundwater is in large parts of the area restricted to a few meters, in particular in lowland areas, which assures strong coupling
157 between groundwater table and evapotranspiration (Maxwell et al., 2007). These typical central European catchment features
158 led us to choose the Neckar catchment as the basis for the virtual catchment.

159 The computational domain is a rectangular area of ~57,850km² encompassing the Neckar catchment of ~14,000km². The
160 domain is larger than the Neckar catchment in order to allow the atmospheric model to develop its own internal dynamics.



161 COSMO is run on a 1.1km horizontal grid with 230x254 grid points, which includes a 4 grid point-wide outer frame zone
162 where only the lateral boundary forcing is used without coupling to the CLM, as well as 50 vertical layers in hybrid coordinates
163 (terrain following at the surface, flat in the stratosphere). COSMO is set up identical to the operational COSMO-DE setup of
164 the German national weather service (Deutscher Wetterdienst, DWD), e.g., the deep convection parameterization is switched
165 off because at the chosen grid resolution convection is enabled by the dynamical core (see Section 2.1). In COSMO-DE, the
166 operational resolution is 2.8km, so that the approximation regarding deep convection is even more appropriate in our
167 simulations. Similar choices were taken by Smith et al. (2015), who simulated precipitation events of roughly the same domain
168 using nested WRF models, where the cumulus parameterization was switched off at horizontal resolutions of 900m and 300m.
169 Lateral boundary forcing and constant fields (topography, land-mask etc.) are provided by the COSMO-DE analysis fields,
170 which are downscaled to the 1.1km grid by linear interpolation. The lateral relaxation zone, which moderates the jump from
171 the lateral driving fields to the inner model area, is set to 12km.

172 A software restriction does not allow for cases with more than 4.2 million CLM columns; thus currently a higher spatial
173 resolution for CLM and ParFlow than 400 m cannot be used for the Neckar catchment. So, ParFlow and CLM use the same
174 horizontal grid with a resolution of 400 m and 535x605 grid points. The vertical grid for both component models is partially
175 the same, with CLM limited to 10 vertical layers up to a total depth of 3 m shared with ParFlow, which has in total 50 vertical
176 layers reaching down to 100m. COSMO runs with a 5sec timestep while CLM and Parflow run at 15min timesteps, which is
177 also the coupling frequency.

178 For setting up CLM, the European digital elevation model (DEM) by the European Environment Agency EEA
179 (<http://www.eea.europa.eu/data-and-maps/data/eu-dem>) was projected to the latitude/longitude grid and bi-linearly
180 interpolated to 400m from the original 30m spatial resolution. The same DEM is used to create the slope input files for ParFlow.
181 A slight modification to the original DEM was made in order to ensure that the simulated Neckar River would flow in the
182 correct valley, especially in the upper half of the catchment where the valley is not always properly resolved by the 400m
183 resolution. In total, the elevation of 8 grid points was reduced to achieve proper routing for the Neckar River. We have not
184 considered rivers outside the Neckar catchment in these corrections; thus there are cases where their routing is not identical to
185 the real rivers.

186 Land use is taken from the 2006 Corine Land Cover Data Set (<http://www.eea.europa.eu/data-and-maps/data/corine-land-cover-2006-raster-3>) also provided by EEA. Since the latter dataset features many more land use types (at a resolution of
187 100m) than required by CLM, they were grouped according to the CLM (IGBP) Plant Functional Type classes (1) broad-leaf
188 forests, (2) needle-leaf forests, (3) grassland, (4) cropland, and (5) bare soil. Urban areas are not considered in this setup and
189 replaced by bare soil. Water surfaces (e.g., larger lakes like Lake Constance in the South of the domain) are also treated as
190 bare soil in CLM while COSMO uses its own land-mask and specific calculations for water surfaces. Therefore, no values
191 from CLM are used for water surfaces in COSMO. A few hundred grid cells feature shrubs (mostly areas that are re- or de-
192 forested or areas at higher altitudes) which are treated as forests, and each grid cell features only one – the most dominant –
193 plant functional type. The plant Leaf Area Index (LAI) is computed from MODIS (Myneni et al. 2002) as monthly averages



195 for the year 2008 for each of the four vegetated land use classes. This LAI is increased for all plant functional types by about
196 20 percent in the summer months and significantly changed from factors less than 1 to about 3.3 in winter-time for needle-leaf
197 forests in order to account for known biases in the MODIS data (Tian et al. 2004). The stem area index (SAI) is estimated from
198 the LAI by a slightly modified (no dead leaves for crops, constant base SAI of 10 percent of the maximum LAI) formulation
199 of Lawrence and Chase (2007) and Zeng et al. (2002) to better represent European tree types. Vegetation height was set to 7m
200 for needle-leaf trees and 10m for broad-leaf trees to account for partial coverage by shrubs, to 20 - 120cm for crops, and to 10
201 - 60 cm for grass depending on the time of the year with low values in the winter months and largest values in July and August.
202 Since we consider only one crop type, we do not specify a harvest date when the plant height drops to its minimum, but assume
203 a smooth decline between August and October.

204 For the representation of soils in CLM we use the 1:1,000,000 soil map (BUEK1000) provided by the Federal Institute for
205 Geosciences and Natural Resources - BGR
206 (http://www.bgr.bund.de/DE/Themen/Boden/Informationsgrundlagen/Bodenkundliche_Karten_Datenbanken/BUEK1000/buek1000_node.html). This soil map is available for entire Germany; thus only small areas in Switzerland and France are missing
207 outside the Neckar catchment for which we assume a nearby soil class. BUEK1000 offers sand and clay percentages as well
208 as carbon content for two to seven soil horizons down to a maximum depth of 3m for each soil type. The carbon content is
209 used to infer soil color. For urban areas (modeled as bare soil, as mentioned above) a fixed soil color (class 8 in CLM) was
210 used.
211

212 Since soil properties may vary substantially at scales smaller than the 1km for which BUEK1000 is appropriate, which might
213 impact system dynamics (Binley et al. 1989, Herbst et al. 2006, Rawls 1983), the soil map is downscaled by artificially adding
214 variability using the conditional points method recently presented in Baroni et al. (2017) as follows:

215 (1) The BUEK1000 soil map is randomly sampled at 1995 point locations with one sample every 5 km² on average, a
216 minimum sample distance of 250 m, and at least one sample for each soil type of the original soil map. This strategy resulted
217 from extensive testing by minimizing the tradeoffs between reproducing the main features of the original soil map and creating
218 variability at finer resolution.

219 (2) The sample locations are used as conditional points for further interpolation. Here, texture, carbon content, and depth
220 of the first three soil horizons are extracted from the BUEK1000. In addition, the sand content of the original map was increased
221 by approximately 20% resulting in a slightly higher hydraulic conductivity because previous simulations yielded too shallow
222 unsaturated zones.

223 (3) Experimental variograms and cross-variograms are calculated for all variables and exponential models were fitted to
224 all spatial structures.

225 (4) A texture map (sand and clay percentage) is generated using a single realization based on conditional co-simulation
226 (Gomez-Hernandez and Journé, 1993) to provide the sub-scale variability (<1 km²). Horizon depths and carbon content are,
227 however, assumed to have a smoothed spatial variability; therefore, they are interpolated based on ordinary kriging.



228 (5) Since ParFlow describes retention and hydraulic conductivity curves based on van-Genuchten-Mualem parameters,
229 pedotransfer functions are applied to estimate these parameters. The pedotransfer functions of Cosby et al. (1984), Rawls
230 (1983) and Tóth et al. (2015) are used and selected based on data availability, applicability of the particular approaches, and
231 previous evaluations conducted in the area (Tietje and Hennings, 1996).

232 In order to keep soil porosity identical between CLM and ParFlow, we replaced the porosity calculation within CLM (which
233 uses a different pedotransfer function). The Manning's surface roughness was set to a constant value of $5.52 \times 10^{-4} \text{ h/m}^{1/3}$ and
234 the specific storage to 1×10^{-3} . The chosen surface roughness value results in a realistic base flow for the local rivers without
235 calibration. Repercussions of this choice are discussed in Chapter 6. Slopes of the main rivers are additionally smoothed to
236 avoid artificial ponded areas.

237 In order to allow for realistic flow in the saturated zone, the 3-D geologic model of the geological survey of the state of Baden-
238 Württemberg was used from which eleven rock types were defined for Baden-Württemberg (see Figure 4). Some characteristic
239 features of the domain, such as middle Triassic and Jurassic karst aquifers, are not included to avoid the manifold hydrological
240 challenges related to its modeling. For areas outside of Baden-Württemberg we extended the rock types at the boundary
241 outwards to cover the full computational domain. Tab. 1 summarizes porosity and hydraulic conductivity used in the domain
242 for the different stratigraphic units. As already mentioned above, karst features of limestones are not considered, and porosities
243 in stratigraphic units containing limestones and crystalline rocks are set considerably higher than in nature to somewhat counter
244 this.

245 Not covered by the discussed data sets are the large alluvial bodies filling large part of the Neckar valley throughout the domain
246 (Riva et al., 2006). Up to 30% of the runoff takes place in the subsurface especially during periods of base flow according to
247 a sub-catchment simulation performed for the year 2007. In that simulation we used measured precipitation and river discharge
248 data together with the simulated evapotranspiration to calculate the water balance over a whole year. While our simulated
249 evapotranspiration rates may be inaccurate, it is implausible that this can account for 30% of the precipitation; i.e. the water
250 could have left the domain only through the subsurface. Thus, gravel channels are needed to account for this lateral flow. Since
251 the valleys in the catchment are often small compared to the limited horizontal resolution of the model, we conceptualize the
252 alluvial bodies as gravel layers underneath all river cells (cells with a mean pressure head $>0.1\text{m}$) and directly next to rivers
253 (riverbanks, i.e., one grid point besides each river cell). The assumed gravel layers reach from beneath the soil down to a depth
254 of 8m. The gravel cells are parameterized with a high hydraulic conductivity of 1 m/h, a porosity of 0.6 and van-Genuchten
255 parameters of 2 for n and 4m^{-1} for α (residual saturation is $0.06 \text{ cm}^3/\text{cm}^3$). Our setup results in a reasonable distribution of
256 surface and subsurface discharge at the outlet of the catchment and reasonable river – aquifer exchange fluxes. In addition to
257 the gravel channels, we included a layer of weathered bedrock, which starts below the soil and extends down to a depth of 6m.
258 This layer is characterized by substantially larger porosity (0.4) and hydraulic conductivity (0.1 m/h) than the rock below. This
259 layer was added to enhance subsurface flow and counter the common occurrence of too shallow water levels if these features
260 are not included.



261 Since we enforce no-flow boundary conditions at the subsurface domain boundaries, all water has to eventually reach the
262 surface in order to leave the domain. This happens predominantly in areas outside of the Neckar catchment, e.g. in the upper
263 Rhine valley, thus soil-moisture values in this region may be too high.

264 **4 Results**

265 In the following, we present example results of the virtual-reality simulations in order to demonstrate its potential for a better
266 understanding of the dynamics in coupled terrestrial systems. We will also show that the simulations quite well resemble
267 observations in the real Neckar catchment, and thus can be used to develop and evaluate modelling and prediction strategies.
268 Precipitation is the strongest hydrological driver in this region; thus its realistic spatial and temporal variability in the domain
269 including its statistical relations with topography is important. Also, the state of the atmospheric boundary layer, which reflects
270 the interaction of the land surface with the atmosphere is a critical component of the terrestrial system, which should be
271 represented by the simulation with some confidence. Along with the comparisons we will also discuss the challenges
272 experienced with such a modeling setup.

273 Figure 5 shows as an example result a snapshot of the simulated three-dimensional distribution of cloud water/ice, precipitation
274 density, and volumetric soil moisture. The soil exhibits different soil moisture layers, the variability of which is mainly
275 connected to different soil hydraulic properties. Only clouds reaching high enough to have sufficient cloud ice produce
276 precipitation, and some precipitation evaporates before it reaches the ground. Extended weather fronts moving through the
277 domain (not shown), which are imposed by the boundary conditions, are also simulated realistically given the resolution of the
278 atmospheric model.

279 **4.1 Relation between water table depth and evapotranspiration**

280 An important measure for hydro-meteorological interactions within a catchment is the relation between water availability and
281 surface energy flux partitioning. Thus, the virtual catchment simulation should capture the expected reduced evapotranspiration
282 (ET) with increasing distance to groundwater (e.g., Maxwell et al., 2007; Shrestha et al., 2014). In Figure 6, we show daily
283 averaged ET (evaporation as all other contributors are zero) values over bare soil against distance to groundwater for 30th April
284 and 30th July for the year 2007. April was almost completely dry (on average less than 3 mm precipitation over the domain),
285 while July was much wetter, but the increased solar radiation and thus temperatures compared to April result in higher ET
286 rates and thus a quicker drying of the top layer of the soil. Figure 6 indicates a reduction in ET when the distance to groundwater
287 falls below 15 – 100cm, depending on soil properties with faster ET reduction for increasing soil sand contents. Such relations
288 are less obvious for cells with significant plant cover: while trees show overall higher ET and almost no ET change with
289 distance to groundwater due to their deep root zones, ET variability increases with larger distances to groundwater (not shown).
290 Also crops and grassland show limited ET changes as a function of distance to groundwater, which can, however, be explained
291 by the high water availability (no water stress) in the time period considered. Figure 6 also contains a small number of grid-



292 points at water table depth of 7m or deeper with evaporation rates only slightly lower than in the shallow water table regions.
293 These relate most likely to cells that retain high levels of upper-level soil moisture even during dry periods to support higher
294 evaporation. This could be either because of the soil properties or due to high flow from neighboring cells. Time-series of soil
295 moisture for the 10 days preceding 30th April and 30th July are shown in Figure 7 to illustrate this effect. It can be seen that
296 volumetric soil moisture for cells with deep water table but high evaporation is much more similar to cells with shallow water
297 table than to cells with deep water table but low evaporation. This means that these cells can retain high upper level soil
298 moisture despite having a low groundwater level. Most of these cells are near rivers and can receive just the right amount of
299 water from lateral flow to keep evaporation high while groundwater level stays low.

300 4.2 Precipitation

301 We compare the simulated precipitation with the 1 km² gridded REGNIE product of DWD, derived from in-situ precipitation
302 observations (Rauthe et al., 2013). For the evaluation of seasonal daily precipitation cycles hourly observations of 71 DWD
303 observational stations are used. The simulated seasonal mean precipitation (Figure 8) and the annual mean precipitation (not
304 shown) are governed by the orographic structures of the Black Forest and Swabian Alb. Values range between approximately
305 520 mm/year around Mannheim and 2105 mm/year over the Black Forest in good accordance with REGNIE concerning the
306 overall pattern and range (510 mm/year – 2130 mm/year). Overall the simulation shows about 10% higher annual precipitation
307 in the east and south and about 25% lower in the north and west compared to REGNIE. During winter (December to February)
308 precipitation is dominated by advection from the west, which result in maxima over the upwind and peak zones of the
309 mountains and leeward minima. The simulated winter pattern (j) compares well with REGNIE (k), but the model
310 underestimates precipitation in the northwestern part of the catchment (l). Over the mountains a slight lateral shift of this kind
311 of precipitation pattern results in neighboring areas with under- and overestimation also found for COSMO simulations coupled
312 to its own TERRA land surface model (e.g., Dierer et al., 2009; Lindau and Simmer, 2013). In fall, the difference pattern
313 between simulations and REGNIE (i) is similar to the winter pattern, but has smaller contrasts. In spring, the simulated
314 precipitation is higher compared to REGNIE. In the summer (June to August), cloud bases are usually higher and reduce the
315 patterns caused by the luff-lee effects. Moist air extends further to the east and south and gets stanchued by the alpine upland
316 leading to enhanced precipitation there. The simulated summer precipitation pattern, which is dominated by convective
317 precipitation, resembles the REGNIE pattern but exceeds the latter by about 20% lower over large parts of the catchment
318 (Figure 8).

319 The mean seasonal diurnal precipitation cycles (Figure 9) reflect the dominating precipitation types. While observed and
320 simulated winter precipitation (Figure 9b) do not show a diurnal cycle, summer precipitation (Figure 9a) increases over the
321 afternoon reaching a maximum at about 7pm in accordance with the maximum of convective precipitation. The simulations
322 reproduce this pattern but exhibit a weak second peak between 6am and 12am while the afternoon/evening increase is delayed
323 by about two hours. The simulated daily precipitation distribution fits the observations quite well. While the virtual catchment
324 has somewhat less dry and low precipitation days than REGNIE, the number of days between 4 and 10 mm are higher than in



325 REGNIE (not shown). The simulated and observed seasonal precipitation cycles (Figure 10) compare very well and mean
326 precipitation is nearly identical between simulations and observations. The model reproduces the seasonal cycle of maximum
327 daily precipitation well, however with larger differences in the summer (see also Dierer et al. 2009).

328 **4.3 Atmospheric State Variables and Surface Radiation**

329 We compare the atmospheric boundary layer (ABL) of the virtual catchment to observations from the meteorological tower at
330 Karlsruhe Institute of Technology (KIT; Kalthoff and Vogel, 1992) and with DWD radiosonde observations in Stuttgart (STG)
331 (see Figure 3 for locations and Table A1 for details of observed quantities). To avoid a biased comparison due to land-cover
332 mismatches between the simulation and the actual land use at the observation sites, the simulations are averaged over five-by-
333 five atmospheric grid boxes centered around the observation sites.

334 The 10m mean diurnal minimum temperatures in the virtual catchment are between 0.5 K (January) and 2.5 K (August) higher
335 than observed (Figure 11, top) and are reached approximately one hour later than observed with the subsequent morning
336 temperature rise shifted accordingly. The simulated diurnal temperature maxima are on average 0.7 K lower than in the
337 observations and are reached 30 minutes later than measured. The morning temperature gradient in the simulation ranges from
338 0.10 K/h in December to 0.31 K/h in April, which compares reasonably well with the observations (0.13/0.52 K/h in
339 January/April). The evening cooling, however, progresses too slowly and results in too high minimum temperatures. At 100
340 m above ground, diurnal maximum temperatures agree within 0.7 K while the warm bias of diurnal minimum temperatures
341 (0.9 K) is smaller than at 10m height (Figure 11, bottom). Also at 100 m a 1h shift between the diurnal minimum temperatures
342 and the morning temperature rise are found. In 200 m height, the simulated monthly mean diurnal cycles are practically
343 identical to the KIT observations (not shown). The temperature standard deviations in the virtual catchment are somewhat
344 smaller than observed, in particular during the afternoon for the summer half year when the reduction can be more than 20%.
345 COSMO in TerrSysMP estimates ABL heights via the bulk Richardson number criterion with a threshold of 0.22 for unstable
346 and 0.33 for stable conditions (Szintai and Kaufmann, 2008). Both seasonal and diurnal variations of the mean ABL height at
347 0 and 12h local time agree well with the observations using the same criterion (Figure 12), but the simulation tends to
348 overestimate ABL heights at nighttime by up to 150 m and underestimate it at daytime by up to 200 m in March. Figure 13
349 compares simulated mean vertical profiles of temperature, virtual potential temperature, and specific humidity with radiosonde
350 observations at 0 h and 12 h local time in Stuttgart (STG) including the mean differences (bias) and the standard deviation of
351 the differences. Simulations are up to 0.9 K warmer close to the surface at 0 h and up to 0.5 K colder at 12 h. At larger heights,
352 the simulations are up to 0.5 K warmer depending on land cover. Specific humidity profiles at 0 h are approximately 0.2 g/kg
353 too dry close to the surface and 0.2 g/kg too wet above 1500 m. At 12 h profiles are up to 0.3 g/kg too wet throughout. The
354 simulations have smaller virtual potential temperature gradients and are thus less stable close to the surface at 0 h. At 12 h, the
355 decreasing virtual potential temperature close to the surface is not captured and tends towards a more neutral instead of unstable
356 profile at low heights.



357 At KIT (STG) the land surface receives on average 20 W/m^2 (5.3 W/m^2) more incoming shortwave radiation and 18 W/m^2 (8
358 W/m^2) less incoming longwave radiation indicating a somewhat lower cloud cover (or lower cloud optical depth) as observed.
359 At daytime (6 h – 22 h), the mean outgoing longwave radiation matches the KIT observations, while at nighttime (22 h – 6 h)
360 values are 7.2 W/m^2 larger than observed, which corresponds to a higher surface temperature of approximately 1.4 K.
361 Overall, the atmospheric profiles, including the ABL heights, compare very well with observations. Noteworthy differences
362 only occur close to the surface with too high nighttime temperatures (up to 2.5 K in summer) and subsequently too small
363 morning temperature gradients. Somewhat higher incoming shortwave and lower incoming longwave radiation at the surface
364 indicate less cloud cover (or lower cloud optical depths) compared to the observations. These results are in line with a previous
365 evaluation of a 2.2 km COSMO simulation (Ban et al. 2014). In addition, we note somewhat reduced unstable conditions at
366 daytime close to the surface in the simulations.

367 **4.4 Passive Microwave Observations**

368 The most direct area-covering observations of soil moisture are currently provided by L-Band (1.4 GHz) passive microwave
369 observations from satellites. The Community Microwave Emission Model (CMEM) is used as a forward operator to simulate
370 the brightness temperatures (TB) at this frequency in vertical and horizontal polarization (de Rosnay et al., 2009). CMEM
371 simulates brightness temperatures at the top of the atmosphere resulting from microwave emission and interaction by soil,
372 vegetation, and atmosphere based on the state variables of the virtual catchment. Input to CMEM are the percentages of clay
373 and sand in the soil, the coverage with open water surfaces, the profiles of soil moisture and soil temperature, vegetation types,
374 and leaf area index (LAI). Satellite orbit geometry, antenna pattern, foot-print and incidence angle are taken into account
375 following the ESA SMOS (Soil Moisture Ocean Salinity) instrument specifications, i.e. a full-width-half-maximum field of
376 view leading to a footprint of 40km across-orbit and 47km along-orbit at multiple incidence angles (Kerr 2001) is applied.
377 This antenna pattern weighs the grid-cell simulated brightness temperatures (Figure 14, left) in order to obtain virtual SMOS
378 observations. Finally, these synthetic observations are rendered according to pixels based on the Icosahedral Snyder Equal
379 Area (ISEA) projection at a spatial separation of about 15 km similar to the SMOS LIC TB data product (Figure 14, right),
380 which can then be compared with real observations for an indirect evaluation of the simulation. Every pixel corresponds to a
381 fixed geo-location of the real SMOS LIC data product over the modeled area. Optionally, the satellite observation operator in
382 TerrSysMP is able to also replicate the NASA SMAP (Soil Moisture Active Passive) radiometer (Saavedra et al., 2016) for
383 years beyond 2015 since when SMAP data is available.

384 We evaluate the simulated brightness temperature distribution over the domain with real SMOS observations between April
385 2011 and September 2011. The real SMOS observations are corrected from radio-frequency interference (RFI) effects over
386 the region following Saavedra et al. (2016). Initial results with CMEM adapted parameters for surface roughness and
387 vegetation optical thickness (which needed to be increased from its standard values found in the literature), lead to a systematic
388 underestimation of the brightness temperature of about -20K on average (see orange line in Figure 15, which compares real



389 SMOS observations with the simulated brightness temperatures) and maximum and minimum differences of -33K and -6K,
390 respectively, for an incidence angle of 30°. A similar underestimation of -14K resulted for the 40° incidence angle with
391 maximum and minimum values of -34K and +15K (lower plot in Figure 16). Those differences are mainly caused by the too
392 large near-surface soil moisture values in the virtual catchment. The cumulative distribution functions of the satellite-derived
393 soil moisture products and the soil moisture of the virtual catchment suggests an about 63% higher near-surface soil moisture
394 compared to the satellite estimates (Saavedra et al. 2016, Figure 6) with extremes of 44% and 95%. A daily matching of the
395 cumulative distribution functions of the virtual catchment and satellite retrieved soil moisture are performed to find a factor
396 which then is assumed to be the soil-moisture bias of the simulation. Figure 16 compares true SMOS observations with
397 simulated brightness temperatures obtained without and with day-to-day correction for the assumed soil-moisture bias of the
398 simulation. The correction decreases the average bias in brightness temperature from -20K(-14K) to about -3K (-2K) for the
399 incidence angle of 30° (40°) at horizontal polarization. Similar results are found when the simulations were statistically
400 compared with observations of later years from the NASA SMAP (Fig. 3 in Saavedra et al. 2016). The remaining bias can
401 probably be further reduced by fine tuning radiation interaction parameters in CMEM, and by including orographic effects on
402 the effective incidence angle. These biases will be addressed by an improved exploitation of the uncertainty of the radiation
403 interaction parameters and by including in CMEM a two-stream approximation to better simulate cases with dense vegetation
404 in the future.

405 The microwave observations retrieved from the virtual catchment show a typical situation encountered in data assimilation;
406 more often than not there are biases between simulated and remote sensing observations. This discrepancy usually has multiple
407 causes, which can relate to the observations themselves, assumptions in the observation operator used to simulate the virtual
408 observations, and in the model used to generate the systems state variables entering the observation operator. Even if these
409 differences cannot be removed, such observations can be highly valuable for data assimilation as long as temporal tendencies
410 are meaningful information. Usually the bias is statistically corrected and thus only the information in the temporal and (if
411 meaningful) spatial variability of the observations is exploited for moving the model states towards the true states.

412 **4.5 Evaluation of River Discharge**

413 We compare river discharge in the virtual catchment with observations made in the Neckar catchment at the gaging stations
414 Rockenau, Lauffen, and Plochingen for a three-year period from 2007 to 2009 (Figure 16). The range of the hydrological
415 response to precipitation in the virtual catchment is in adequate agreement with the observations; this is noteworthy since no
416 calibration to runoff data has been applied to the model. The simulated discharge peaks are, however, higher and delayed by
417 about one to three days compared to the observations. A reason could be a too large Manning's coefficient and the model
418 resolution. In the discussion we suggest a scaling of Mannings coefficient to account for the mismatch between true river width
419 and the model resolution in order to better represent realistic flood dynamics. In spring and summer, the response to
420 precipitation is significantly smoother than observed and peak amplitudes vary with respect to peak amplitudes of the



421 observations. The differences between observed and simulated precipitation discussed above and the effects of the less
422 predictable convective events during these seasons may also play a significant role. Convective events will always be displaced
423 in space and time compared to the observations and may even show different individual life cycles including lifetime and
424 amplitude. Finally, the base flow is much lower compared to the real catchment during dry periods, most likely because the
425 grid resolution is considerably larger than the actual river width and the unresolved subsurface spatial heterogeneity. An
426 increased hydraulic conductivity via an increased soil sand content may reduce the base flow further as infiltration increases.
427 The results are further evaluated comparing the flow duration curve and the monthly runoff coefficient. The former represents
428 the statistical probability to exceed a specific discharge value within a given time period while the latter is the ratio between
429 runoff and precipitation over the catchment area. Figure 17 shows the lower exceedance probability of the virtual catchment
430 compared to the observations, in particular for low discharge rates, a behavior attributed to the lower base flow component
431 and confirmed by the too low runoff coefficients in spring and summer but similar coefficients during the rest of the year
432 (Figure 18). We hypothesize that in this period the simulation has a lower hydrological response also due to missing subsurface
433 heterogeneity. As stated above, we have neglected karst features, which are known to produce fast lateral subsurface flows.
434 Overall, the model captures the general statistical features of the catchment including the typical seasonal trends quite well,
435 while differences are noted related to hydrological extremes and base flow. These differences could be reduced by model
436 calibration from which we refrain because hydrological extremes are not primary the objective of this study. We discuss
437 options to improve the representation of river discharge further below.

438 **4.6 Groundwater**

439 A plausibility check of the groundwater levels is performed in two steps. First we visually inspect the groundwater depth map,
440 shown in Figure 19a. Accordingly, the model shows a good distribution between shallower and deeper (5 meter and below)
441 groundwater tables. Furthermore, the deeper sections are found in the mountainous areas of the model domain, which
442 corresponds well with the real situation. It has to be noted though that regions with shallow groundwater levels often show
443 very small values, likely not to be found in the real catchment where the unsaturated zone is usually thicker. In a second step,
444 we compare simulated hydraulic heads with available data. The environmental protection agency of the state of Baden-
445 Württemberg (Landesanstalt für Umwelt, Messungen und Naturschutz – LUBW) operates 33 continuous groundwater
446 observation wells. Comparing those point measurements to simulation results of an uncalibrated model with 400m grid
447 resolution makes little sense. Instead, we compare (1) the magnitude of the fluctuation in the groundwater table throughout the
448 catchment during a year (calculated as the groundwater observation minus its mean, shown in Figure 19b) and (2) the average
449 trend of the groundwater in the full model (calculated after subtracting the mean and scaling the fluctuations to have the same
450 magnitude. According to Figure 19c, the magnitude of the groundwater fluctuations are within similar ranges as the
451 observations (Figure 19b), while a few real observation wells show larger magnitudes. Also the trends overall follow similar
452 patterns (Figure 19c). Hence, the groundwater, given the coarse resolution of the model in comparison with the compared point
453 measurements, shows a reasonable behavior.



454 5 Discussion

455 The size of the catchment and resolution considered (400 m) pose an enormous challenge in terms of required CPU-time. Still,
456 the applicability of Darcy's law with laboratory-based parameters can be debated as we have to resort to apparent model
457 parameters to produce realistic mass fluxes in the compartments. By compromising these technical and physical aspects in the
458 setup of the virtual catchment, we experienced several challenges; four of them will be discussed which we believe to be
459 inherent to simulating energy and mass fluxes across compartment boundaries with partial-differential-equation-based, high-
460 resolution coupled models.

461 **Representation of rivers and surface roughness:** River flow in the ParFlow module of TerrSysMP is simulated by an
462 overland flow module. Overland flow appears when hydraulic heads in the top cells are above the land surface. As there is no
463 discrimination between overland flow and river flow, rivers in the simulation have the width of the grid resolution whereas the
464 real rivers may be significantly narrower. Overland flow is represented in ParFlow with the kinematic wave approximation of
465 the St. Venant equations with the surface friction parameterized by Manning's coefficient. Typical Manning's coefficients
466 when assigned to e.g. to a 400 m grid cell while in fact the river is much narrower, would result in too high discharge values
467 during rain events and far too low ones during dry periods. In both cases the always too low water levels caused by the too
468 wide rivers result in a poor representation of river-subsurface exchange. Our current choice of Manning's coefficient in
469 ParFlow ($5.52 \times 10^{-4} \text{ h/m}^{1/3}$) results in realistic average discharge throughout the year, albeit at too low flow velocities. In order
470 to compensate for this inconsistency, the Manning's coefficient could be scaled such that the overland flow velocity in river
471 cells equals the river flow velocity as proposed by Schalge et al. (2019), which improves the phasing between simulated and
472 observed discharge and the discharge peak. Similarly, the hydraulic conductivity of the model top layer for river cells could
473 be scaled in order to reduce the loss of too much surface water to the subsurface caused by the too wide river cells. These
474 issues will become even more severe when model resolutions are reduced, e.g., for ensemble-based data assimilation because
475 of the even higher demands for computing efficiency.

476 **Coarsening of topography:** The still coarse topography of the virtual catchment reduces the true hill slopes where lateral flow
477 on the surface and in the shallow subsurface takes place. This affects quick-flow components towards rivers. As shown by
478 Shrestha et al. (2015), coarse topography directly impacts the storage of water in the unsaturated zone because drainage
479 becomes less effective. This in turn can lead to an overestimation of latent and underestimation of sensible heat flux.
480 Additionally, coarse-resolution model runs result in delayed and stretched discharge peaks in the rivers. The severity of this
481 effect is proportional to the degree of topography smoothing, that is introduced by the coarser resolution; therefore, any change
482 in subsurface parameters such as hydraulic conductivity will depend on the degree of coarsening and the location within a
483 catchment. Especially in narrow valleys and in mountainous areas this will lead to an overestimation of soil moisture, which
484 we have not yet compensated by changing other parameters. Recently a method has been proposed to improve these issues by
485 scaling horizontal hydraulic conductivity (Foster and Maxwell, 2019).



486 **Soil parameters:** As outlined in section 2, the soil hydraulic parameters were generated based on soil maps of the real Neckar
487 catchment. According to the maps, the soils in the catchment consist mainly of clay and silt, which have rather low saturated
488 hydraulic conductivities and small air entry pressure values. In large areas of the domain, the water content in our first
489 simulations was close to saturation, even for upper soil layers, and the infiltration velocities were unrealistically low. Reasons
490 are the soil parameters, which do not capture the true soil heterogeneity; moreover, real infiltration often takes place in root
491 channels, small fractures, and other small structures. Thus, infiltration is always underpredicted by models using observed soil
492 parameters assuming homogeneity. Infiltration processes may be better captured with dual domain approaches, which are,
493 however, computationally demanding. A workaround would be to change the soil hydraulic parameters in order to obtain
494 stronger infiltration. Currently, we use an artificially increased sand percentage of the soils in order to stay consistent with the
495 concept of the pedotransfer functions used in CLM. We will also test known scaling rules (e.g., Ghanbarian et al., 2015) to
496 increase for example the saturated hydraulic conductivity for larger soil units. These rules should be applied on the soil
497 hydraulic parameters, estimated by the pedotransfer functions.

498 **6 Conclusions and Outlook**

499 In the present study we show the development and the data generated based on a integrated subsurface-land surface-atmosphere
500 system TSMP. Plausibility tests for the derived virtual reality which tries to mimic the Neckar catchment in southwestern
501 Germany, show that the virtual catchment is able to reproduce realistic behavior when compared to measurements.
502 Comparisons of simulated precipitation and ABL statistics show a very reasonable agreement with real observations. However,
503 comparisons with observed passive microwave measurements by satellites shows clearly a systematic bias which is probably
504 related to a mixture of systematic errors in the latter, assumptions in the used forward operator, parameterizations of land
505 surface properties (soil parameters) in the simulation, and missing processes therein (e.g., preferential flow, hill-slope
506 processes). The analysis also shows a realistic connection between evapotranspiration and distance to groundwater in the
507 virtual catchment, while larger deviations from reality are found for river discharge dynamics. The deficiencies could be traced
508 to the model resolution, which limits the often much smaller river widths to multiples of the model resolution, and to the way
509 river discharge is handled in the ParFlow component of TerrSysMP. A new parameterization scheme proposed by Schalge et
510 al. (2019) will avoid such problems in future model simulations. The main issues we face for the upper Neckar are too high
511 soil moisture and shallow groundwater levels. Several ideas have been proposed to improve the setup including scaling of the
512 surface roughness and soil parameters.

513 Overall the results are encouraging regarding the viability of the virtual reality as key input parameters to the land surface and
514 subsurface show very good agreement with observations. For these reasons, the analysis show that the results can be used as
515 a basis for the community for, among others, exploring feedbacks between compartments, identify in which conditions
516 simplification of the models could be done (Baroni et al., 2019) or develop and test methods for assimilating observations
517 across compartments . We encourage the scientific community to explore this data for the different applications. Within the



518 study we also highlighted some limitations mainly due to the still sever technical limitation and the IT-requirements. We
519 anticipate however that more sophisticated versions of the virtual catchment (higher resolution, improved parameterization of
520 sub-scale processes as discussed above) are already in progress that could be also compared to this virtual reality in further
521 study.

522

523 **7 Data Availability**

524 The presented virtual catchment is available in the CERA database of the German Climate Computing Center (DKRZ:
525 Deutsches Klimarechenzentrum GmbH) (Schalge et al., 2020) at https://doi.org/10.26050/WDCC/Neckar_VCS_v1. The full
526 nine-year time series (2007-2015) for all three compartments has a size of roughly 40TB in compressed netCDF4 format.
527 Nevertheless, we encourage the use of this data set for investigations on data assimilation, but also the general functioning of
528 catchments including cross-environmental interactions and predictability studies can profit from such complete state evolutions
529 of the regional Earth system.

530 The TerrSysMP model is built in a modular way and users are supposed to get the component models by themselves while the
531 coupling interface is provided through a git repository (<https://git.meteo.uni-bonn.de>). As of now, registration is required to
532 access the TerrSysMP git and wiki page.

533 Both ParFlow (<https://parflow.org/>) and CLM (<http://www.cgd.ucar.edu/tss/clm/distribution/clm3.5/>) are freely available for
534 download from their respective websites or repositories. COSMO is not available, but the DWD supplies it free of charge for
535 research purposes upon request. More information on this process can be found in the TerrSysMP wiki.

536

537 **Acknowledgements**

538 This research is funded by the Deutsche Forschungsgemeinschaft (DFG, FOR2131: "Data Assimilation for Improved
539 Characterization of Fluxes across Compartmental Interfaces"). The authors gratefully acknowledge the Gauss Centre for
540 Supercomputing e.V. (www.gauss-centre.eu) for funding this project by providing computing time through the John von
541 Neumann Institute for Computing (NIC) on the GCS Supercomputer JUQUEEN at Jülich Supercomputing Centre (JSC). We
542 thank the members of HPSC-TerrSys (http://www.hpsc-terrsys.de/hpsc-terrsys/EN/Home/home_node.html) and Klaus
543 Goergen in particular for invaluable technical support with the JUQUEEN supercomputer. Furthermore, we thank Prabhakar
544 Shresta and Mauro Sulis for their preliminary work and introduction to the TerrSysMP modeling platform. We also
545 acknowledge work done on an earlier version of this script by Jehan Rihani.

546 **References**

547 Alkama, R., Papa, F., Faroux, S., Douville, H., and Prigent, C.: Global off-line evaluation of the ISBA–TRIP flood model,
548 *Climate Dyn.*, 38, 1389–1412, doi:10.1007/s00382-011-1054-9, 2012.



- 549 Ashby, S.F., and Falgout R. D.: A parallel multigrid preconditioned conjugate gradient algorithm for groundwater flow
550 simulations, Nuclear Science and Engineering, 124(1), 145-159,1996.
- 551 Avissar, R., and Pielke, R. A.: A parameterization of heterogeneous land surfaces for atmospheric numerical models and its
552 impact on regional meteorology. Monthly Weather Review, 117(10), 2113-2136, doi:10.1175/1520-
553 0493(1989)117<2113:APOHLS>2.0.CO;2,1989.
- 554 Baldauf, M., Seifert, A., Foerstner, J., Majewski, D., Raschendorfer, M., and Reinhardt, T.: Operational convective-scale
555 numerical weather prediction with the COSMO model: description and sensitivities. Monthly Weather Review, 139(12), 3887-
556 3905, doi:10.1175/MWR-D-10-05013.1,2011.
- 557 Ban, N., Schmidli, J., and Schaer, C.: Evaluation of the convection-resolving regional climate modelling approach in decade-
558 long simulations. J. Geophys. Res. Atmos., 119, 7889–7907, doi:10.1002/2014JD021478,2014.
- 559 Baroni, G., Schalge, B., Rakovec, O., Kumar, R., Schüler, L., Samaniego, L., Simmer, C., Attinger, S.: A comprehensive
560 distributed hydrological modelling inter-comparison to support processes representation and data collection strategies. Water
561 Resources Research. <https://doi.org/10.1029/2018WR023941>, 2019
- 562 Baroni, G., Zink, M., Kumar, R., Samaniego, L., Attinger, S.: Effects of uncertainty in soil properties on simulated hydrological
563 states and fluxes at different spatio-temporal scales. Hydrol. Earth Syst. Sci. 21, 2301–2320. [https://doi.org/10.5194/hess-21-
564 2301-2017](https://doi.org/10.5194/hess-21-2301-2017), 2017.
- 565 Bashford, K. E., Beven, K. J., and Young, P. C.: Observational data and scale-dependent parameterizations: explorations using
566 a virtual hydrological reality. Hydrological Processes 16, 293–312. doi:10.1002/hyp.33,2002.
- 567 Binley, A., Elgy, J., and Beven, K.: A physically based model of heterogeneous hillslopes: 1. Runoff production. Water
568 Resources Research, 25, 1219–1226. doi:10.1029/WR025i006p01219,1989.
- 569 Chan, S., Njoku, E., and Colliander, A.: SMAP LIC Radiometer Half-Orbit 36 km EASE-Grid Brightness Temperatures.
570 Version 2. Boulder, Colorado USA: NASA National Snow and Ice Data Center Distributed Active Archive Center.
571 doi:10.5067/Y9C3Q3060AZ5,2015.
- 572 Chaney, N. W., Roundy, J. K., Herrera-Estrada, J. E., and Wood, E. F. (2015): High-resolution modeling of the spatial
573 heterogeneity of soil moisture: Applications in network design. Water Resources Research 51, 619–638.
574 doi:10.1002/2013WR014964,2015.
- 575 Clark, M. P., Fan, Y., Lawrence, D. M., Adam, J. C., Bolster, D., Gochis, D. J., Hooper, R. P., Kumar, M., Leung, L. R.,
576 Mackay, D. S., Maxwell, R. M., Shen, C., Swenson, S. C. and Zeng, X.: Improving the representation of hydrologic processes
577 in Earth system models. Water Resources Research, 51, 5929–5956. <https://doi.org/10.1002/2015WR017096>, 2015
- 578 Cosby, B. J., Hornberger, G. M., Clapp, R. B., and Ginn, T. R.: A Statistical Exploration of the Relationships of Soil Moisture
579 Characteristics to the Physical Properties of Soils. Water Resour. Res., 0, 682–690. doi:10.1029/WR020i006p00682,1984.
- 580 de Rosnay, P., Drusch, M., Boone, A., Balsamo, G., Decharme, B., Harris, P., Kerr, Y., Pellarin, T., Polcher, J., and Wigneron,
581 J. P.: AMMA Land Surface Model Intercomparison Experiment coupled to the Community Microwave Emission Model:
582 ALMIP-MEMP. Journal Geophysical Research, 114, D05108, doi:10.1029/2008JD010724,2009.



- 583 Davison, J.H., Hwang, H.-T., Sudicky, E.A., Mallia, D.V., Lin, J.C.: Full Coupling Between the Atmosphere, Surface, and
584 Subsurface for Integrated Hydrologic Simulation. *Journal of Advances in Modeling Earth Systems*.
585 <https://doi.org/10.1002/2017MS001052>, 2018
- 586 Dierer, S., Arpagaus, M., Seifert, A., Avgoustoglou, E., Dumitrache, R., Grazzini, F., Mercogliano, P., Milelli, M., and
587 Starosta, K.: Deficiencies in quantitative precipitation forecasts: sensitivity studies using the COSMO model. *Meteorologische*
588 *Zeitschrift*, 18 (6), 631-645, doi:10.1127/0941-2948/2009/0420,2009.
- 589 Foster, L.M., Maxwell, R.M., 2019. Sensitivity analysis of hydraulic conductivity and Manning's n parameters lead to new
590 method to scale effective hydraulic conductivity across model resolutions. *Hydrological Processes* 33, 332–349.
591 <https://doi.org/10.1002/hyp.13327>
- 592 Gasper, F., Goergen, K., Shrestha, P., Sulis, M., Rihani, J., Geimer, M., and Kollet, S.: Implementation and scaling of the fully
593 coupled Terrestrial Systems Modeling Platform (TerrSysMP) in a massively parallel supercomputing environment-a case study
594 on JUQUEEN (IBM Blue Gene/Q). *Geoscientific model development discussions*, 7, 3545-3573, doi:10.5194/gmdd-7-3545-
595 2014,2014.
- 596 Gomez-Hernandez, J., Journel J., and Journel, A. G.: Joint Sequential Simulation of MultiGaussian Fields, in Troia '92,
597 Amilcar Soares (Ed.), volume 1, pages 85-94, Kluwer Academic Publishers,1993.
- 598 Fatichi, S., Vivoni, E. R., Ogden, F. L., Ivanov, V. Y., Mirus, B., Gochis, D., Downer, C. W., Camporese, M., Davison, J. H.,
599 Ebel, B., Jones, N., Kim, J., Mascaro, G., Niswonger, R., Restrepo, P., Rigon, R., Shen, C., Sulis, M., and Tarboton, D.: An
600 overview of current applications, challenges, and future trends in distributed process-based models in hydrology. *J. Hydrol.*
601 537, 45–60. doi:10.1016/j.jhydrol.2016.03.026,2016.
- 602 Ghanbarian, B., Taslimitehrani, V., Dong,, G., and Pachepsky, Y. A.: Sample dimensions effect on prediction of soil water
603 retention curve and saturated hydraulic conductivity. *Journal of Hydrology*. 528,127-137,
604 doi:10.1016/j.jhydrol.2015.06.024,2015.
- 605 Haeffliger, V., Martin, E., Boone, A., Habets, F., David, C. H., Garambois, P.-A., Roux, H., Ricci, S., Berthon, L., Thévenin,
606 A., and Biancamaria, S.: Evaluation of Regional-Scale River Depth Simulations Using Various Routing Schemes within a
607 Hydrometeorological Modeling Framework for the Preparation of the SWOT Mission, *Journal of Hydrometeorology*, 16,
608 1821-1842, doi:10.1175/JHM-D-14-0107.1,2015.
- 609 Hein, A., Condon, L., Maxwell, R.M.: Evaluating the relative importance of precipitation, temperature and land-cover change
610 in the hydrologic response to extreme meteorological drought conditions over the North American High Plains. *Hydrology*
611 *and Earth System Sciences* 23, 1931–1950. <https://doi.org/10.5194/hess-23-1931-2019>, 2019
- 612 Hendricks Franssen, H. J., Alcolea, A., Riva, M., Bakr, M., Van der Wiel, N., Stauffer, F., and Guadagnini, A.: A comparison
613 of seven methods for the inverse modelling of groundwater flow. Application to the characterisation of well catchments, *Adv.*
614 *Water. Resour.*, 32 (6), 851-872, doi:10.1016/j.advwatres.2009.02.011,2009.
- 615 Herbst, M., Diekkrueger, B., and Vanderborght J.: Numerical experiments on the sensitivity of runoff generation to the spatial
616 variation of soil hydraulic properties. *Journal of Hydrology*, 326, 43–58. doi:10.1016/j.jhydrol.2005.10.036,2006.



- 617 Jones, J. E., and Woodward C. S.: Newton–Krylov-multigrid solvers for large-scale, highly heterogeneous, variably saturated
618 flow problems. *Advances in Water Resources*, 24(7), 763-774, 2001.
- 619 Jülich Supercomputing Centre. JUQUEEN: IBM Blue Gene/Q Supercomputer System at the Jülich Supercomputing Centre.
620 *Journal of large-scale research facilities*, 1, A1. doi:10.17815/jlsrf-1-18, 2015.
- 621 Kalthoff, N., and Vogel, B.: Counter-current and channelling effect under stable stratification in the area of Karlsruhe. *Theor.*
622 *Appl. Climatol.*, 45(2), 113-126, doi:10.1007/BF00866400,1992.
- 623 Kerr, Y H, Waldteufel, P, Wigneron, J P, Front, J and Berger, M: Soil moisture retrieval from space: The soil moisture and
624 ocean salinity (SMOS) mission. *IEEE Trans. Geosci. Re. Sens.*, 39(8): 1729–1735. DOI:<https://doi.org/10.1109/36.942551>,
625 2001.
- 626 Kollet, S. J., and Maxwell, R. M.: Integrated surface–groundwater flow modeling: A free-surface overland flow boundary
627 condition in a parallel groundwater flow model. *Advances in Water Resources*, 29(7), 945-958,
628 doi:10.1016/j.advwatres.2005.08.006,2006.
- 629 Kollet, S. J., Maxwell, R. M., Woodward, C. S., Smith, S., Vanderborght, J., Vereecken, H., and Simmer, C.: Proof of concept
630 of regional scale hydrologic simulations at hydrologic resolution utilizing massively parallel computer resources. *Water*
631 *Resources Research*, 46(4), doi:10.1029/2009WR008730,2010.
- 632 Kurtz, W., He, G., Kollet, S. J., Maxwell, R. M., Vereecken, H., and H. Franssen, H.-J.: TerrSysMP-PDAF version 1.0): a
633 modular high-performance data assimilation framework for an integrated land surface-subsurface model. *Geoscientific Model*
634 *Development*, 9(4), 1341-1360, doi:10.5194/gmd-9-1341-2016,2016.
- 635 Larsen, M. A. D., Refsgaard, J. C., Drews, M., Butts, M. B., Jensen, K. H., Christensen, J. H., and Christensen, O. B.: Results
636 from a full coupling of the HIRHAM regional climate model and the MIKE SHE hydrological model for a Danish catchment,
637 *Hydrol. Earth Syst. Sci.*, 18, 4733-4749, doi:10.5194/hess-18-4733-2014, 2014.
- 638 Lawrence, P. J., and Chase, T. N.: Representing a new MODIS consistent land surface in the Community Land Model (CLM
639 3.0). *J. Geophys. Res.*, 112, G01023, doi:10.1029/2006JG000168,2007.
- 640 Lindau, R., and Simmer C.: On correcting precipitation as simulated by the regional climate model COSMO-CLM with daily
641 rain gauge observations. *Meteorology and Atmospheric Physics*, 119, 1-2, p.31-42, doi:10.1007/s00703-012-0215-7,2013.
- 642 Mackay, E. B., Wilkinson, M. E., Macleod, C. J. A., Beven, K., Percy, B. J., Macklin, M. G., Quinn, P. F., Stutter, M., and
643 Haygarth, P. M.: Digital catchment observatories: A platform for engagement and knowledge exchange between catchment
644 scientists, policy makers, and local communities. *Water Resour. Res.*, 51(6), 4815-4822. doi:10.1002/2014WR016824,2015.
- 645 Maxwell R. M., Chow F. K., Kollet S. J.: The groundwater-land-surface-atmosphere connection: Soil moisture effects on the
646 atmospheric boundary layer in fully-coupled simulations, *Advances in Water Resour.*, 30(12), 2447-2466, 2007
- 647 Myneni, R. B., Hoffman, S., Knyazikhin, Y., Privette, J. L., Glassy, J., Tian, Y., Wang, Y., Song, X., Zhang, Y., Smith, G. R.,
648 Lotsch, A., Friedl, M., Morisette, J. T., Votava, P., Nemani, R. R., and Running, S. W.: Global products of vegetation leaf area
649 and fraction absorbed PAR from year one of MODIS data. *Remote Sensing of Environment*, 83(1), 214-231,
650 doi:10.1016/S0034-4257(02)00074-3,2002.



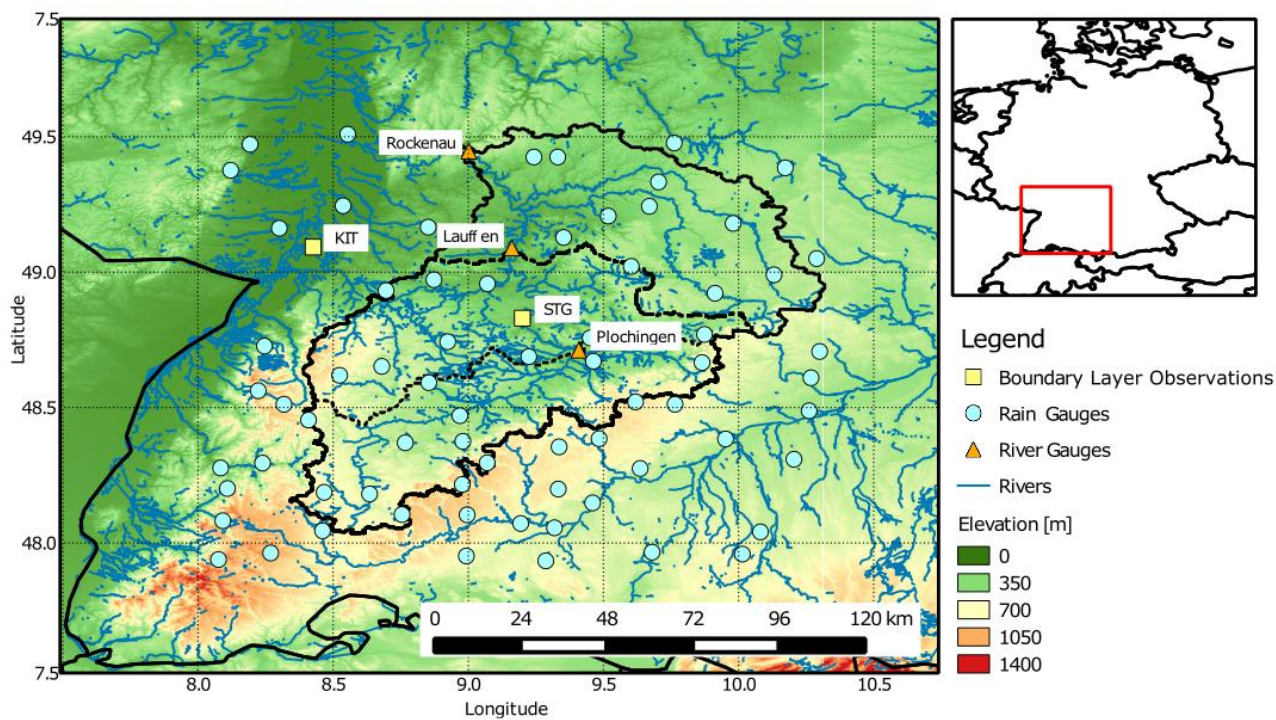
- 651 Oleson, K. W., Niu, G. Y., Yang, Z. L., Lawrence, D. M., Thornton, P. E., Lawrence, P. J., and Qian, T.: Improvements to the
652 community land model and their impact on the hydrological cycle. *Journal of Geophysical Research: Biogeosciences* (2005–
653 2012), 113(G1), doi:10.1029/2007JG000563,2008.
- 654 Poltoradnev, M., Ingwersen, J., and Streck, T.: Spatial and temporal variability of soil water content in two regions of
655 Southwest Germany during a three-year observation period. *Vadose Zone Journal*, 15(6), doi:10.2136/vzj2015.11.0143,2016.
- 656 Rauthe, M., Steiner, H., Riediger, U., Mazurkiewicz, A., and Gratzki, A. (2013): A Central European precipitation climatology
657 – Part I: Generation and validation of a high-resolution gridded daily data set (HYRAS), Vol. 22(3), p 235–256,
658 doi:10.1127/0941-2948/2013/0436,2013.
- 659 Rawls, W. J.: Estimating soil bulk density from particle size analysis and organic matter content. *Soil Sci.*, 135 (2), 123-
660 125,1983.
- 661 Ridler, M. E., van Velzen, N., Hummel, S., Sandholt, I., Falk, A. K., Heemink, A., and Madsen, H.: Data assimilation
662 framework: linking an open data assimilation library (OpenDA) to a widely adopted model interface (OpenMI), *Environ.*
663 *Modell. Softw.*, 57, 76–89, doi:10.1016/j.envsoft.2014.02.008, 2014.
- 664 Riva, M., Guadagnini, L., Guadagnini, A., Ptak, T., and Martac, E. (2006): Probabilistic study of well capture zones distribution
665 at the Lauswiesen field site. *J. Contam. Hydrol.* 88, 92–118, doi:10.1016/j.jconhyd.2006.06.005,2006.
- 666 Saavedra P., Simmer, C., and Schalge, B.: Evaluation of modeled high resolution soil moisture virtual brightness temperature
667 compared to space-borne observations for the Neckar catchment. *IEEE Xplore 14th Specialist Meeting on Microwave*
668 *Radiometry and Remote Sensing of the Environment (MicroRad)*, pp. 85-90, doi:10.1109/MICRORAD.2016.7530510,2016.
- 669 Saavedra, P. and Simmer, C.: An Octave/MATLAB® Interface for Rapid Processing of SMOS L1C Full Polarization
670 Brightness Temperature. *Journal of Open Research Software*, 6, 1, p.2, DOI: <http://doi.org/10.5334/jors.165>, 2018
- 671 Schaefer, D., Dahmke, A., Kolditz, O., and Teutsch, G.: Virtual Aquifers: A Concept for Evaluation of Exploration,
672 Remediation and Monitoring Strategies. In: *Calibration and Reliability in Groundwater Modelling: A Few Steps Closer to*
673 *Reality (Proceedings of the ModelCARE 2002 Conference held in Prague, Czech Republic, June 2002)*, edited by K. Kovar,
674 Z. Hrkal, IAHS Publication 277, IAHS Press Oxfordshire, pp. 52-59,2002.
- 675 Schalge, B., Haeflinger, V., Kollet, S., and Simmer, C: Improvement of surface runoff in the hydrological model ParFlow by a
676 scale-consistent river parameterization. Accepted for publication in *Hydrological Processes*, 2019.
- 677 Schalge, Bernd; Baroni, Gabriele; Haese, Barbara; Erdal, Daniel; Geppert, Gernot; Saavedra, Pablo; Haeflinger, Vincent;
678 Vereecken, Harry; Attinger, Sabine; Kunstmann, Harald; Cirpka, Olaf A.; Ament, Felix; Kollet, Stefan; Neuweiler, Insa;
679 Hendricks Franssen, Harrie-Jan; Simmer, Clemens (2020). Virtual catchment simulation based on the Neckar region. World
680 Data Center for Climate (WDCC) at DKRZ. https://doi.org/10.26050/WDCC/Neckar_VCS_v1
- 681 Schlueter, S., Vogel, H.-J., Ippisch, O., Bastian, P., Roth, K., Schelle, H., Durner, W., Kasteel, R., and Vanderborght, J.: Virtual
682 soils: assessment of the effects of soil structure on the hydraulic behavior of cultivated soils. *Vadose Zone Journal* 11,
683 doi:10.2136/vzj2011.0174,2012.



- 684 Schomburg, A., Venema, V., Lindau, R., Ament, F., and Simmer, C.: A downscaling scheme for atmospheric variables to
685 drive soil–vegetation–atmosphere transfer models. *Tellus B*, 62(4), 242–258, doi:10.1111/j.1600-0889.2010.00466.x,2010.
- 686 Schomburg, A., Venema, V., Ament, F., and Simmer, C.: Disaggregation of screen-level variables in a numerical weather
687 prediction model with an explicit simulation of subgrid-scale land-surface heterogeneity. *Meteorology and Atmospheric
688 Physics*, 116(3-4), 81–94, doi:10.1007/s00703-012-0183-y,2012.
- 689 Semenova, O., and Beven, K.: Barriers to progress in distributed hydrological modelling: Invited commentary. *Hydrological
690 Processes*, 29(8), 2074–2078. <https://doi.org/10.1002/hyp.10434>
- 691 Shi, Y., Davis, K. J., Zhang, F., Duffy, C. J., and Yu, X.: Parameter estimation of a physically based land surface hydrologic
692 model using the ensemble Kalman filter : A synthetic experiment, *Water Resources Research*, 50(1), 706–724,
693 doi:10.1002/2013wr014070,2014.
- 694 Shi, Y., Davis, K. J., Zhang, F., Duffy, C. J., and Yu, X.: Parameter estimation of a physically-based land surface hydrologic
695 model using an ensemble Kalman filter: A multivariate real-data experiment, *Advances in Water Resources*, 83, 421–427,
696 doi:10.1016/j.advwatres.2015.06.009,2015.
- 697 Shrestha, P., Sulis, M., Masbou, M., Kollet, S., and Simmer, C.: A scale-consistent terrestrial systems modeling platform
698 based on COSMO, CLM, and ParFlow. *Monthly Weather Review*, 142(9), 3466–3483, doi:10.1175/MWR-D-14-
699 00029.1,2014.
- 700 Shrestha, P., Sulis, M., Simmer, C., Kollet, S.: Impacts of grid resolution on surface energy fluxes simulated with an integrated
701 surface-groundwater flow model, *Hydrol. Earth Syst. Sci.*, 19, 4317–4326, doi:10.5194/hess-19-4317-2015,2015.
- 702 Simmer, C., Thiele-Eich, I., Masbou, M., Amelung, W., Crewell, S., Diekkrueger, B., Ewert, F., Hendricks Franssen, H.-J.,
703 Huisman, A. J., Kemna, A., Klitzsch, N., Kollet, S., Langensiepen, M., Loehnert, U., Rahman, M., Rascher, U., Schneider, K.,
704 Schween, J., Shao, Y., Shrestha, P., Stiebler, M., Sulis, M., Vanderborght, J., Vereecken, H., van der Kruk, J., Zerenner, T.,
705 and Waldhoff, G.: Monitoring and Modeling the Terrestrial System from Pores to Catchments - the Transregional
706 Collaborative Research Center on Patterns in the Soil-Vegetation-Atmosphere System. *Bulletin of the American
707 Meteorological Society*, 96, 1765–1787. doi:10.1175/BAMS-D-13-00134.1,2015.
- 708 Smith, V. H., Mobbs, S. D., Burton, R. R., Hobby, M., Aoshima, F., Wulfmeyer, V., and Di Girolamo, P.: The role of orography
709 in the regeneration of convection: A case study from the convective and orographically-induced precipitation study.
710 *Meteorologische Zeitschrift*, Vol. 24, No. 1, 83–97, doi:10.1127/metz/2014/0418,2015.
- 711 Sulis, M., Langensiepen, M., Shrestha, P., Schickling, A., Simmer, C., and Kollet, S. J.: Evaluating the influence of plant-
712 specific physiological parameterizations on the partitioning of land surface energy fluxes. *Journal of Hydrometeorology*, 16(2),
713 517–533, doi:10.1175/JHM-D-14-0153.1,2015.
- 714 Szintai, B., and Kaufmann, P.: TKE as a measure of turbulence. *COSMO Newsletter* 8, 2–9,2008.
- 715 Tian, Y., Dickinson, R. E., Zhou, L., Zeng, X., Dai, Y., Myneni, R. B., Knyazikhin, Y., Zhang, X., Friedl, M., Yu, I., Wu, W.,
716 and Shaikh, M.: Comparison of seasonal and spatial variations of leaf area index and fraction of absorbed photosynthetically

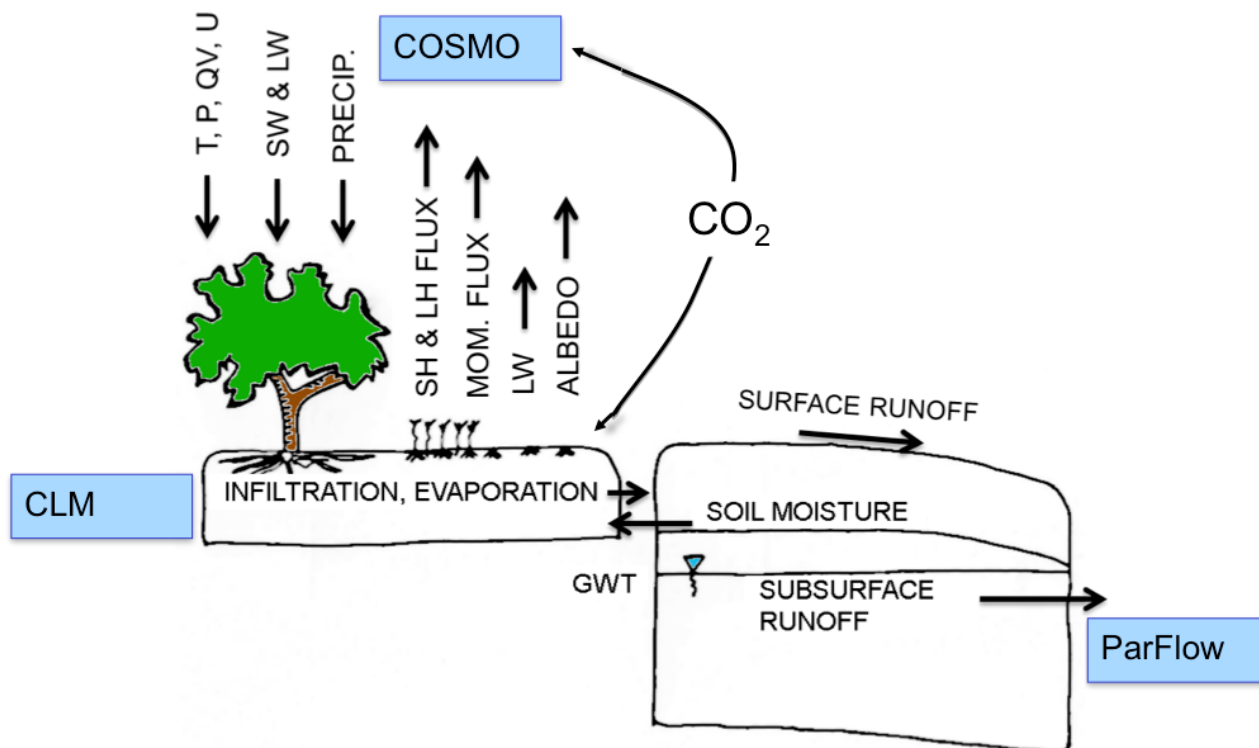


- 717 active radiation from Moderate Resolution Imaging Spectroradiometer (MODIS) and Common Land Model. *J. Geophys. Res.*,
718 109, D01103, doi:10.1029/2003JD003777,2004.
- 719 Tietje, O., and Hennings, V.: Accuracy of the saturated hydraulic conductivity prediction by pedo-transfer functions compared
720 to the variability within FAO textural classes. *Geoderma*, 69, 71–84. doi:10.1016/0016-7061(95)00050-X,1996.
- 721 Tóth, B., Weynants, M., Nemes, A., Makó, A., Bilas, G., and Tóth, G.: New generation of hydraulic pedotransfer functions
722 for Europe: New hydraulic pedotransfer functions for Europe. *Eur. J. Soil Sci.*, 66, 226–238. doi:10.1111/ejss.12192,2015.
- 723 Valcke, S.: OASIS3 PRISM Model Interface Library: OASIS3 User Guide. PRIMS Support Initiative, Report No. 3,2006.
- 724 Weiler, M., and McDonnell, J.: Virtual experiments: a new approach for improving process conceptualization in hillslope
725 hydrology. *Journal of Hydrology* 285, 3–18. doi:10.1016/S0022-1694(03)00271-3,2004.
- 726 Zeng, X., Shaikh, M., Dai, Y., Dickinson, R. E., Myneni, R.: Coupling of the common land model to the NCAR community
727 climate model. *J. Climate* 15, 1832–1854, doi:10.1175/1520-0442(2002)015<1832:COTCLM>2.0.CO;2,2002.
- 728 Zimmerman, D. A., G. de Marsily, G., C.A. Gotway, C. A., M.G. Marietta, M. G., C.L. Axness, C. L., R.L. Beauheim, R. L.,
729 Bras, R. L., Carrera, J., Dagan, G., Davies, P. B., Gallegos, D. P., Galli, A., Gomez-Hernandez, J., Grindrod, P., Gutjahr, A.
730 L., Kitanidis, P. K., Lavenue, A. M., McLaughlin, D., Neuman, S. P., RamaRao, B. S., Ravenne, C., and Rubin, Y.: A
731 comparison of seven geostatistically based inverse approaches to estimate transmissivities for modeling advective transport by
732 groundwater flow, *Water Resour Res* 34(6), 1373-1413, doi:10.1029/98WR00003,1998.
- 733



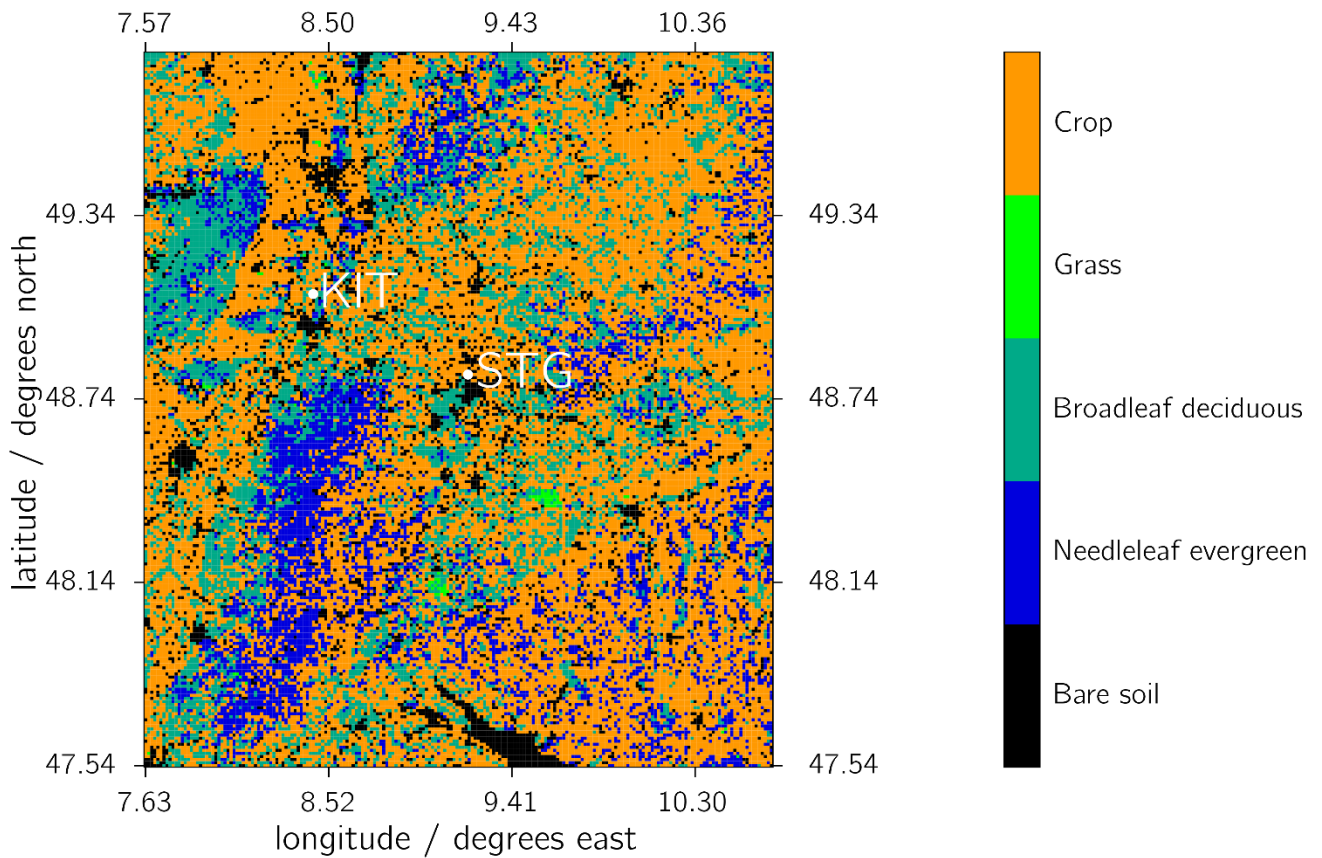
734
735 **Figure 1: Location of the Neckar catchment within SW Germany.**

736



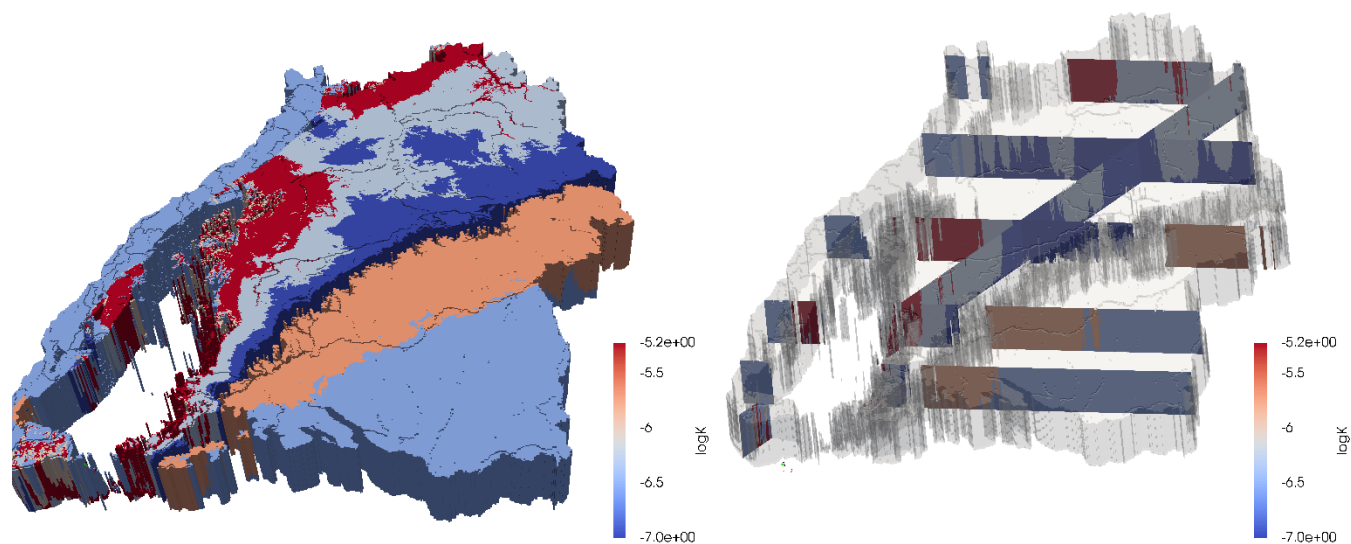
737
738
739

Figure 2: Exchange of energy and mass fluxes in TerrSysMP (Gasper et al., 2014).



740
741
742

Figure 3: Land cover in Domain 1 covering the entire Neckar catchment and bounding areas. KIT: Karlsruhe Institute of Technology (location of meteorological tower observations), STG: Stuttgart (location of radiosonde observations).



743

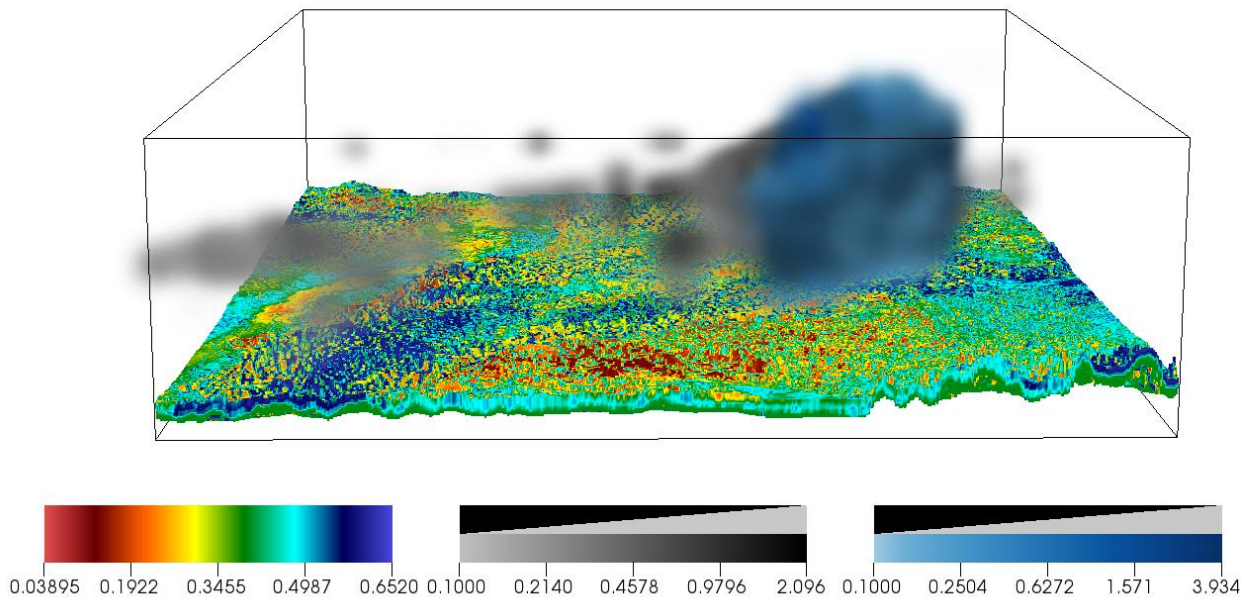
744

745

746

747

Figure 4: Stratigraphy in the state of Baden-Württemberg represented by its logarithmic conductivity. The left figure shows a 3-D view of the 100 m deep geological model used in this work, where the elevation has been neglected for readability and the transparent regions corresponds to low-permeable material. The right figure shows the same using cross-sections to better visualize the vertical heterogeneity.

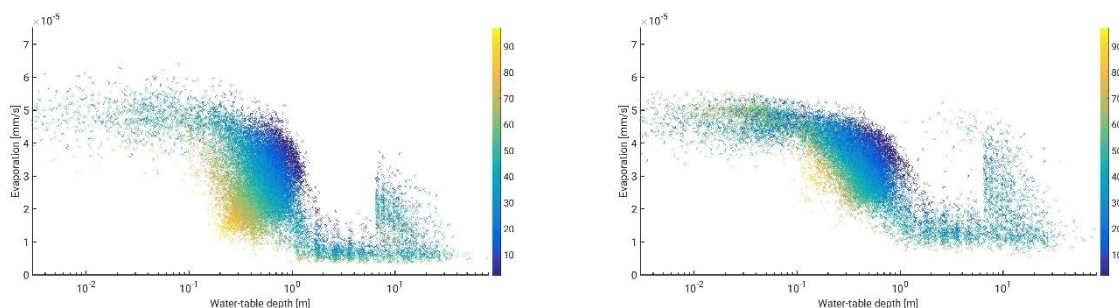


748

749

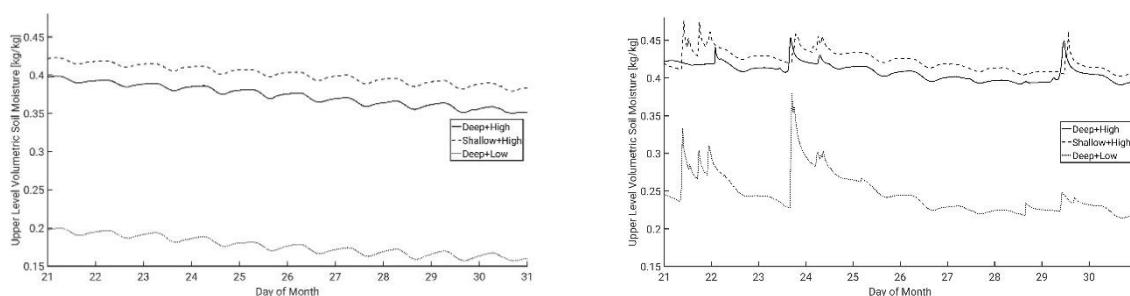
750

Figure 5: Snapshot of the three dimensional distribution of cloud water/ice [g/kg] (greyscale), precipitation/rain water [g/kg] (blue in foreground over cloud) and soil moisture [cm³/cm³] at a time point with a single rain cloud with light rain.



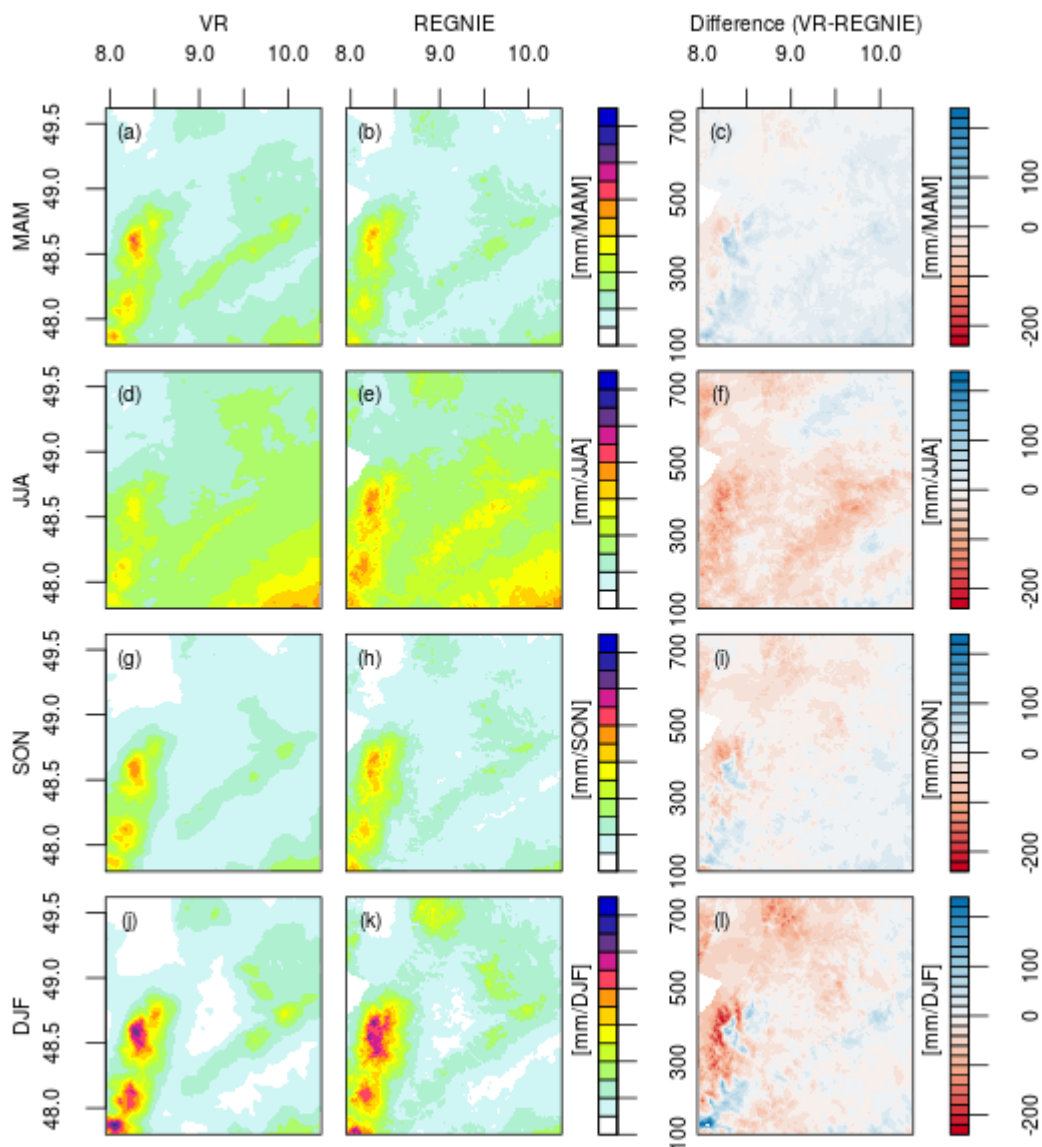
751
752
753

Figure 6: Daily average evapotranspiration (ET) simulated for 30th April (left) and 30th July 2007 in [mm/day]. The color indicates soil sand percentage.



754
755
756
757
758

Figure 7: 10-day time-series of volumetric soil moisture for three representative grid-points with high evaporation and shallow water-table (Shallow+High), low evaporation and deep water-table (Deep+Low), and high evaporation and deep water-table (Deep+High) prior to the days shown in Figure 6.

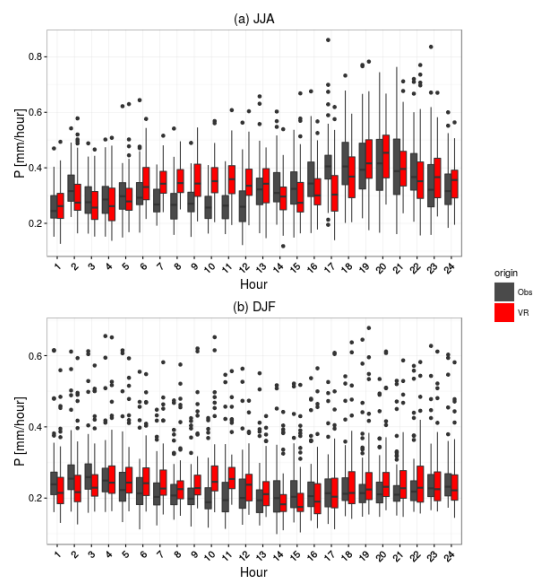


759

760 **Figure 8: Mean seasonal precipitation over the Neckar catchment between 2007-2013 in the virtual reality (VR, left column)**
761 **compared to the REGNIE data set (middle column). The difference between VR and REGNIE is shown in the right column. Figure**
762 **(a), (b), and (c) show the comparison for spring (March – May); (d), (e), and (f) for summer (June – August); (g), (h), and (i) for fall**
763 **(September – November); and (j), (k), and (l) for winter (December-February).**

764

765



766

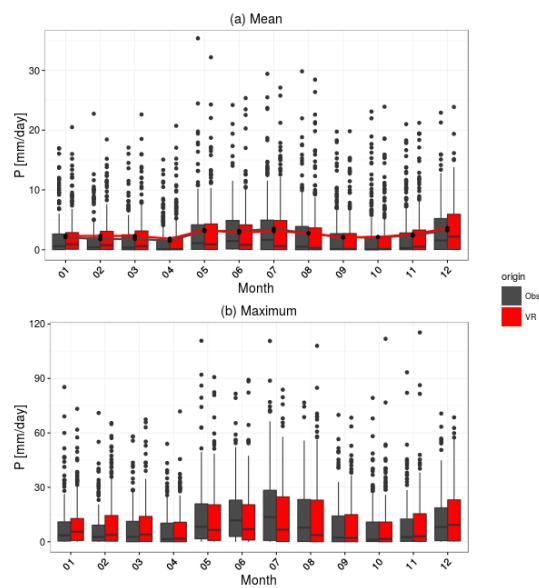
767

768

769

770

Figure 9: Mean diurnal precipitation cycle for the 71 DWD stations and the corresponding simulations for wet days (more than 1 [mm/day]) for June-August (a) and December-February (b) season. The upper and lower hinges correspond to the first and third quartile, the center black line the median, the upper whisker (analog for lower whisker) extends from the hinge to the highest value within 1.5*(interquartile range), and the black dots mark the outliers.



771

772

773

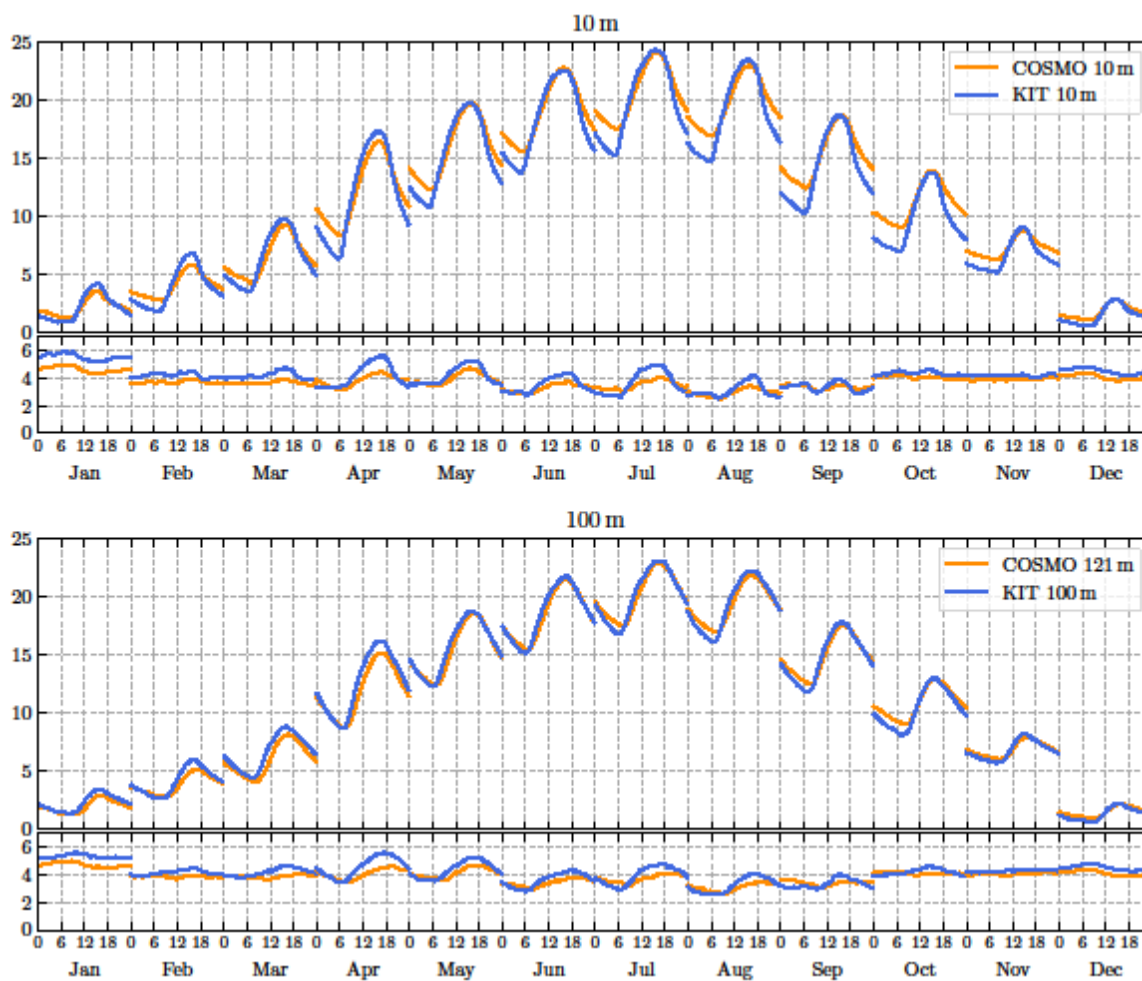
774

775

Figure 10: (a) Daily precipitation distribution on a monthly basis as observed (black) and simulated (red). The gray and red lines indicate the monthly mean precipitation. (b) Maximum daily precipitation for the given months for the 71 DWD stations and the corresponding simulation. Box sizes as explained in the caption of Figure 10.

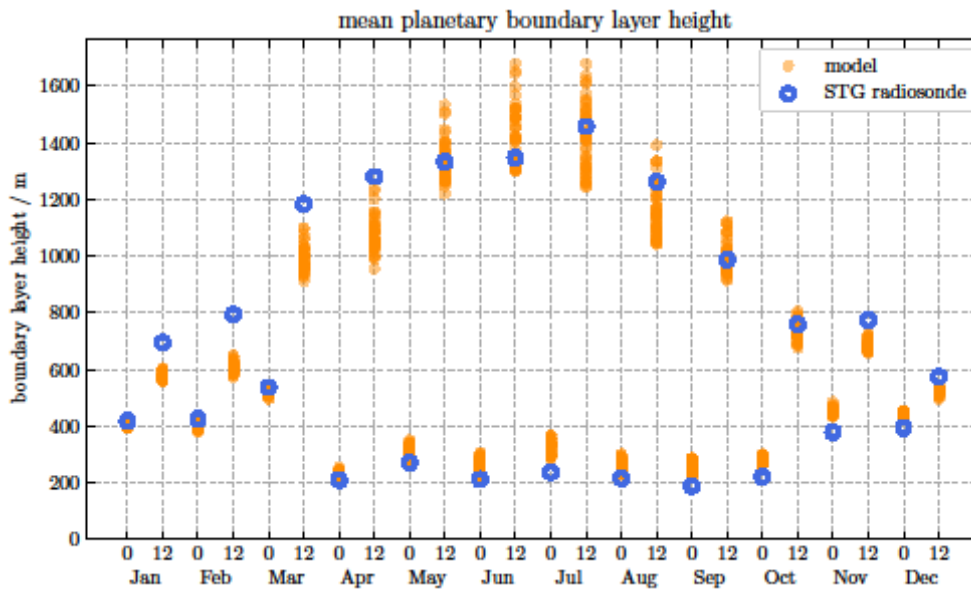
776

777



778
779

780 **Figure 11: Monthly mean diurnal cycles (local time) and respective standard deviation for air temperature in 10 m (top) and 100 m**
781 **(bottom) height at the KIT tower and for the COSMO grid boxes around the KIT location.**

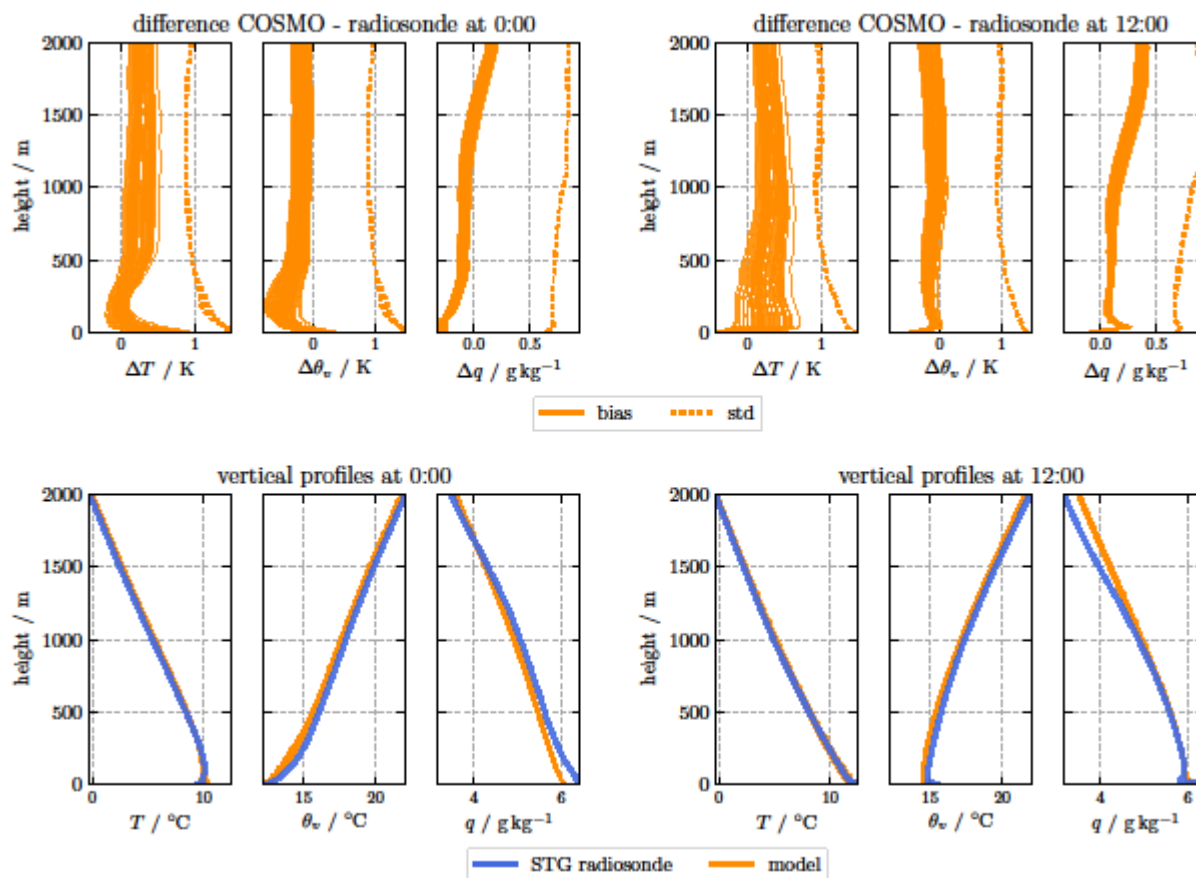


782

783

784

Figure 12: Monthly mean boundary layer height at 0 h and 12 h local time for different land covers diagnosed from radiosonde observations at Stuttgart STG and from atmospheric profiles above grid boxes of CLM.



785

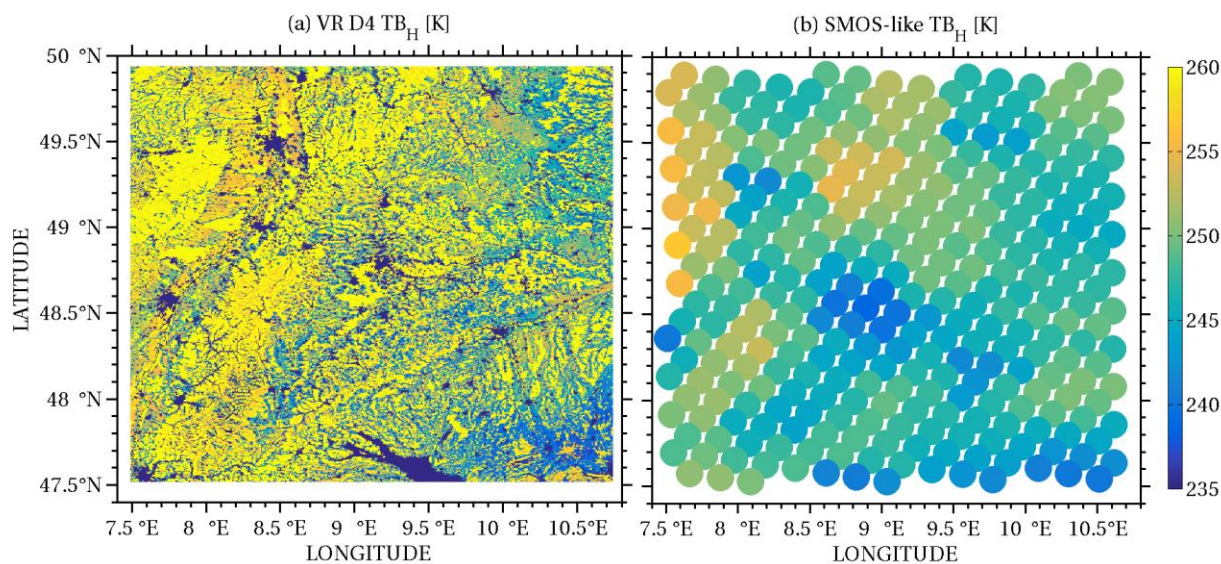
786

787

788

789

Figure 13: Mean vertical profiles of temperature, virtual potential temperature, and specific humidity (top), and mean differences between modelled and observed data including the standard deviation of the differences (bottom). The experimental data are from the radiosonde data at STG and the simulated data from the grid boxes of the virtual catchment with different land cover (left: 0 h local time, right: 12 h local time).

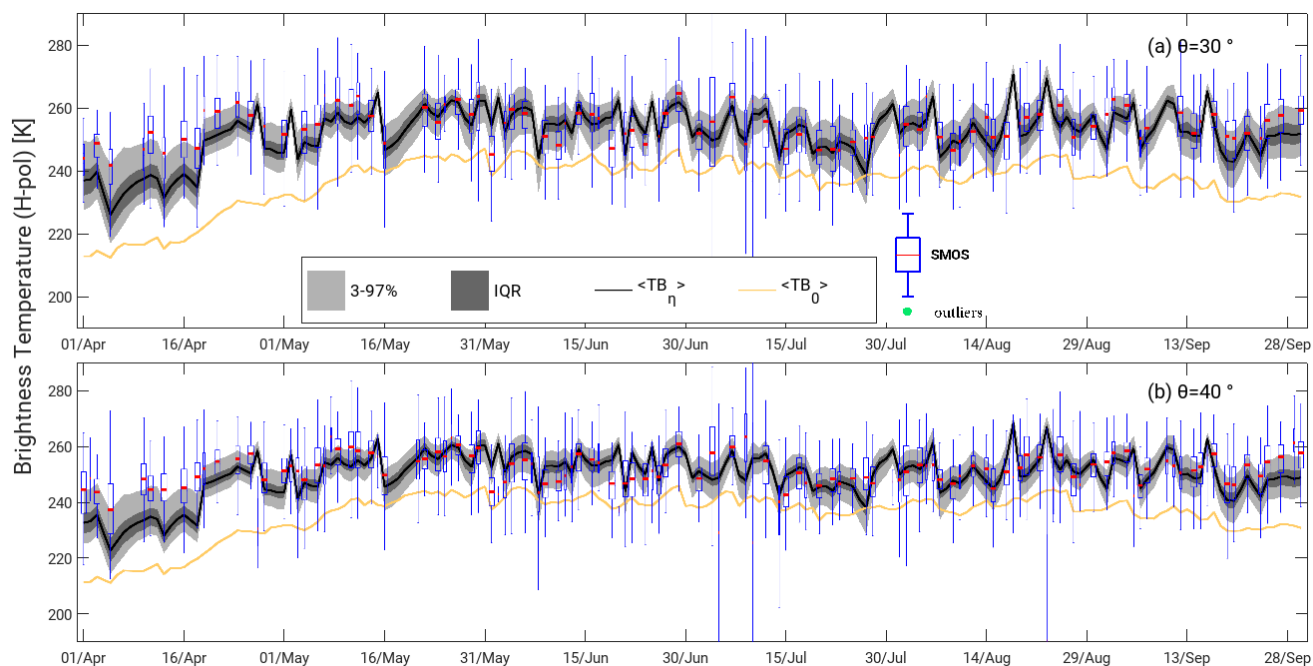


790

791

792

Figure 14: Brightness temperature calculated by the application of CMEM (H-polarization) on the virtual-reality output on July 2nd 2011 (left) and its aggregation on the spatial resolution of the LIC data-product SMOS passive microwave radiometer (right).



793

794

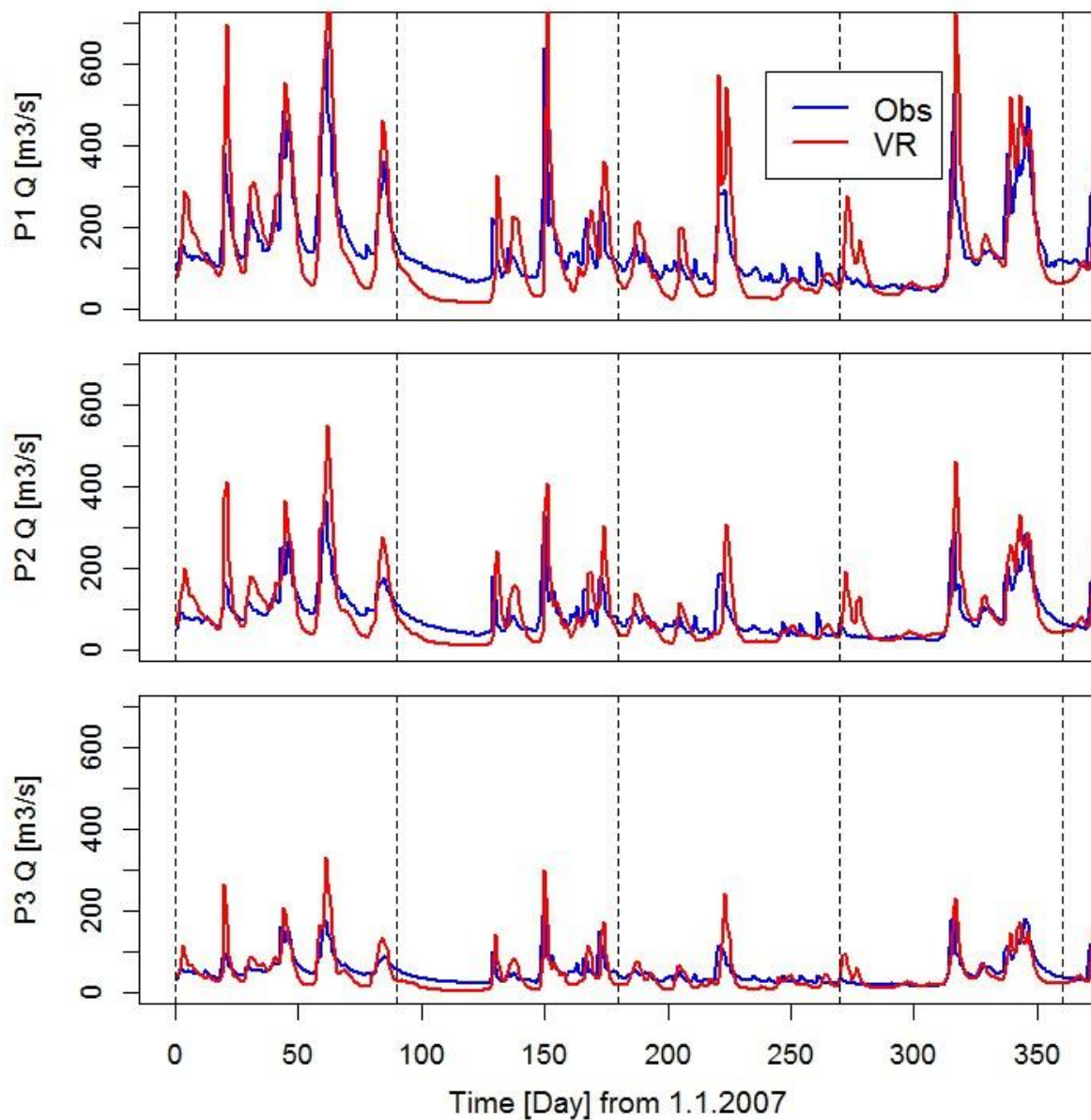
795

796

797

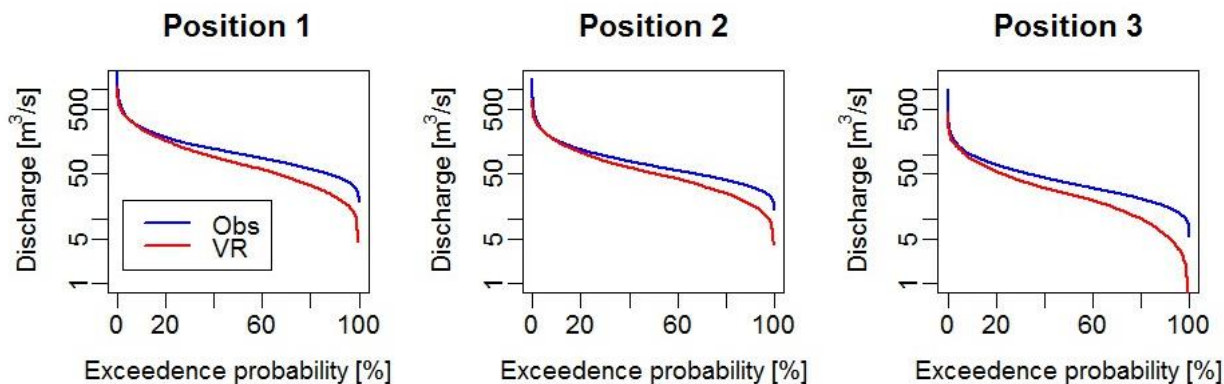
798

Figure 15: Area-averaged L-band brightness temperature the period from April to September 2011 for an incidence angle of 30° (top) and 40° (bottom). The boxplots indicate the real SMOS observations averaged over the same domain. The black line is the median of the virtual observations simulated with CMEM. The dark-gray area corresponds to the inter-quartile range (IQR) while the light-gray area encompasses the 3 to 97% range. The orange continuous line indicates the brightness temperature without taking into account an assumed bias in surface soil moisture content (see text).



799
800
801

Figure 16: Hourly values river discharge at the gauging stations Rockenau (P1), Lauffen (P2) and Plochingen (P3) for the year 2007. Blue: observed; red: virtual catchment.

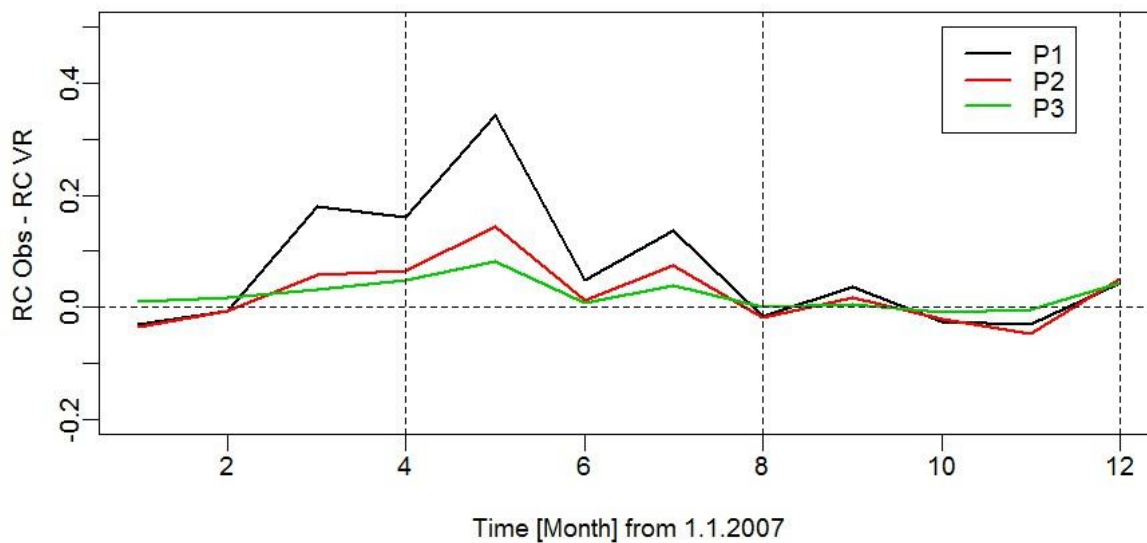


802

803

804

Figure 17: Flow duration curve for the three stations for the three year time period based on. Blue: observations; red: virtual catchment.

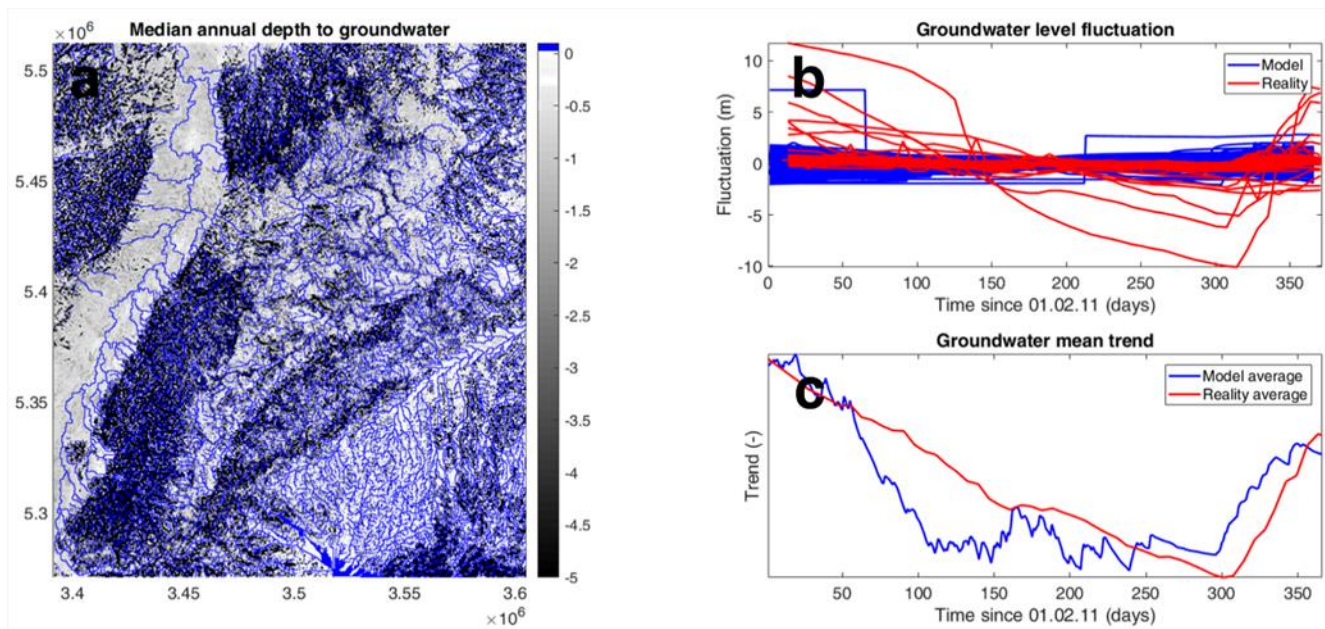


805

806

807

Figure 18: Differences between the run off coefficient calculated for the three stations for the year 2007 based on observations and virtual catchment.



808

809 **Figure 19:**(a) Mean groundwater table depth of the entire domain for the year ranging from 01.02.11 to 01.02.12, (b) groundwater
810 fluctuations around a zero mean and (c) the total mean of all model cells and all real data points superimposed on top of each other
811 to show the annual average trend. Please note that for readability of the figure, subfigure (a) is limited to a maximum depth of -5 m,
812 while the underlying data ranged down to -88 m

813

814

815

816

817

818



819 **Appendix**

820 **7.1 Appendix Tables**

821 **Table A1: Values of porosity and hydraulic conductivity of rocks found in Baden-Wuerttemberg**

Nr.	rock type	Ksat [m/h]	porosity fraction
1	Quaternary	0.00100	0.3
2	Tertiary	0.00100	0.3
3	Upper Jura	0.00720	0.3
4	Middle Jura	10^{-7}	0.3
5	Lower Jura	10^{-7}	0.3
6	Upper Triassic (Keuper)	0.00036	0.3
7	Middle Triassic (Muschelkalk)	0.00180	0.3
8	Lower Triassic (Buntsandstein)	0.02160	0.4
9	Upper Permian (Rotliegendes)	0.00360	0.3
10	New Red Conglomerate	0.00100	0.3
11	Bedrock/Granite	10^{-7}	0.3

822

823



824

825 **Table A2: Observed atmospheric variables at KIT and STG. Local time at STG is UTC+01.**

826

dataset	quantity	temporal resolution	height above ground	data coverage
KIT	temperature	10 min averages (resampled to 15 min)	10 m, 100 m	01/2007 – 12/2013
	Incoming and outgoing shortwave radiation		-	
	Incoming and outgoing longwave radiation		-	06/2011 – 12/2013
STG	temperature	12 h (11:45 h and 23:45 h local time)	vertical profiles (interpolated to model levels)	01/2007 – 12/2013
	dew point temperature			
	pressure			
	incoming shortwave radiation	1 h averages	-	
	incoming longwave radiation		-	

827

828

829

830